Tritium Science Program FY17 Report:

Fundamental Studies of Tritium Solubility and Diffusivity in $LiAlO_2$ and Lithium Zirconates Pellets Used in TPBAR

Hari P. Paudel, Yueh-Lin Lee, Jamie Holber,
Dan C. Sorescu, and Yuhua Duan

September 29, 2017

DOE/NETL-PUB-21464

DISCLAIMER

Table of Contents

List of Figures

List of Tables

1. Introduction

In tritium-producing burnable absorber rods (TPBARs), due to its high-density, the $LiAlO_2$ is used in the form of an annular ceramic pellet enriched with the ^{6}Li isotope and is located between the zircaloy-4 liner and nickel-plated zircaloy-4 tritium getter. When irradiated in a pressurized water reactor (PWR), the ^{6}Li pellets absorb neutrons, simulating the nuclear characteristics of a burnable absorber rod, and produce tritium ($^{3}_{1}T$). The $^{3}_{1}T$ chemically reacts with the metal getter, which upon capture of the $^{3}_{1}T$ becomes a metal hydride. The $^{3}_{1}T$ can then be recovered from the metal hydride. The $^{3}_{1}T$ transport through the ceramic pellets and the barrier/cladding system will affect the performance of the TPBARs, but the understanding of this process is hampered by a lack of fundamental data such as hydrogen isotope solubility and diffusivity.

1.1 Project Technical Scope

Using atomistic level calculations, in this study, we propose to investigate the solubility and diffusivity properties of hydrogen isotopes in the blanket candidate materials (e.g. Li_2O, $LiAlO_2$, Li_2ZrO_3, $Li_6Zr_2O_7$, Li_8ZrO_6, Li_4SiO_4, *etc*.) for TPBARs to enable tritium production in PWRs and to improve the performances of these components.

With the knowledge of $^{3}_{1}T$ transport, the potential impact of the candidate performance mechanisms of the pellet materials can be evaluated computationally. Using results from our previously performed research on the electronic and thermodynamic properties of these ceramic materials, we will study the $^{3}_{1}T$ diffusivity and solubility in the abovementioned lithium ceramic materials. Lithium zirconates are stable at very high temperatures and have high densities and ion conductivities. These materials can also be used as pellets which may result in a better overall performance in TPBAR. Lithium zirconates contain lithium-rich phases, such as $Li_6Zr_2O_7$, Li_8ZrO_6, which may result in a high ^{6}Li density to minimize the ^{6}Li enrichment. The focus of current research is to identify the mechanisms associated with atomic $^{3}_{1}T$ formation, diffusion, transport, deposition, and the kinetics at high temperature.

For these purposes, we will employ first-principles density functional theory (DFT) and molecular dynamics (MD) simulations to perform our investigations. The project can be divided into four tasks:

- **Task 1**: Project initiation. We will collect the relevant information about ${}_{1}^{3}T$ diffusion in pellet materials including the crystal structure, thermodynamic and self-diffusion properties, plus the corresponding electronic structure properties, by searching the literature on these ceramic materials ($LiAlO_2$, Li_2ZrO_3, $Li_6Zr_2O_7$, and Li_8ZrO_6).
- **Task 2**: By combining DFT with lattice phonon dynamics, the thermodynamic properties of the pure and defective materials versus temperatures will be evaluated. Since their bulk properties have been previously investigated by us, we will focus on the effects of defects on the thermodynamic properties of $LiAlO_2$ and Li_2ZrO_3 to prepare for further diffusion and solubility calculations.
- **Task 3**: After irradiation (${}_{3}^{6}Li + n \rightarrow {}_{1}^{3}T + \alpha$), various defects will be created in the pellets. In order to explore the ${}_{1}^{3}T$ diffusivity and solubility in these defective pellet, we will first explore the defect chemistry of the $LiAlO_2$ and Li_2ZrO_3 as well as Li_2TiO_3 for comparison to previous literature results then investigate the formation of ${}_{1}^{3}T$ to see which ${}_{1}^{3}T$ species (ionic, atomic, radical (OT^-), T_2 molecule) dominate for the diffusion. The outcome of these investigations is to obtain the necessary information for the next task, namely to explore the mechanisms on how ${}_{1}^{3}T$ species diffuse in the pellet and move to ${}_{1}^{3}T$ getter layer for capture. Due to the large demand on computing resources, only two cases ($LiAlO_2$, Li_2ZrO_3) will be studied.
- **Task 4**: By calculating the ${}_{1}^{3}T$ species diffusion barriers and the mechanisms in pure and defective bulk materials ($LiAlO_2$, Li_2ZrO_3, ($Li_6Zr_2O_7$, and Li_8ZrO_6)), the corresponding diffusivities of ${}_{1}^{3}T$ in these ceramic materials will be obtained. From these results, several sets of results will be drawn, such as the comparison of the ${}_{1}^{3}T$ species diffusivity and solubility before and after point defect creation, whether high-Li content materials can affect the ${}_{1}^{3}T$ diffusivity and solubility, and the corresponding diffusion pathways of ${}_{1}^{3}T$ species.

In this report, we present our results on calculations of bulk properties, defect chemistry, and diffusion in γ-$LiAlO_2$ and Li_2ZrO_3. Understanding of Li diffusion in ceramic blanket material is crucial to properly address the tritium release behavior and performance of the material as tritium diffusivity can be correlated with the Li hopping mechanism. The study of Li diffusivity in Li containing ceramics has also been a subject of interest in the areas of Li-ion battery and solid oxide fuel cells. Several experimental and theoretical efforts have been made in an attempt to understand the Li diffusion mechanism in γ- $LiAlO_2$. A powerful experimental technique to understand atomic diffusion in crystals is the nuclear magnetic resonance (NMR) measurements as a function of temperature. With the known value of spin-lattice relaxation from NMR measurements, it is possible to calculate ionic jump rate τ^{-1} that allows us to calculate a diffusion coefficient using Einstein−Smoluchowski equation. Using NMR and dc conductivity measurements in γ- $LiAlO_2$, it was revealed that the Li diffusion coefficient was in the range 10^{-20} to 10^{-13} m^2/s over the temperature range of 400 K to 1000 K. Based on the use of NMR techniques and dc conductivity measurements the activation energy was found to vary between 0.74 to 1.14 eV (see section 4). In the literature, based on DFT, the Li activation energy was calculated in γ- $LiAlO_2$ and shown to be 0.65 eV, 1.65 eV and 1.41 eV, respectively for the jump between 1st, 2nd and 3rd nearest neighbor (NN) (see section 4). Our study will focus on identifying the mechanisms of substitutional, interstitial and correlated motions of ${}^3_1T$ and Li in γ- $LiAlO_2$ and Li_2ZrO_3.

1.2 Project Schedule/Milestones

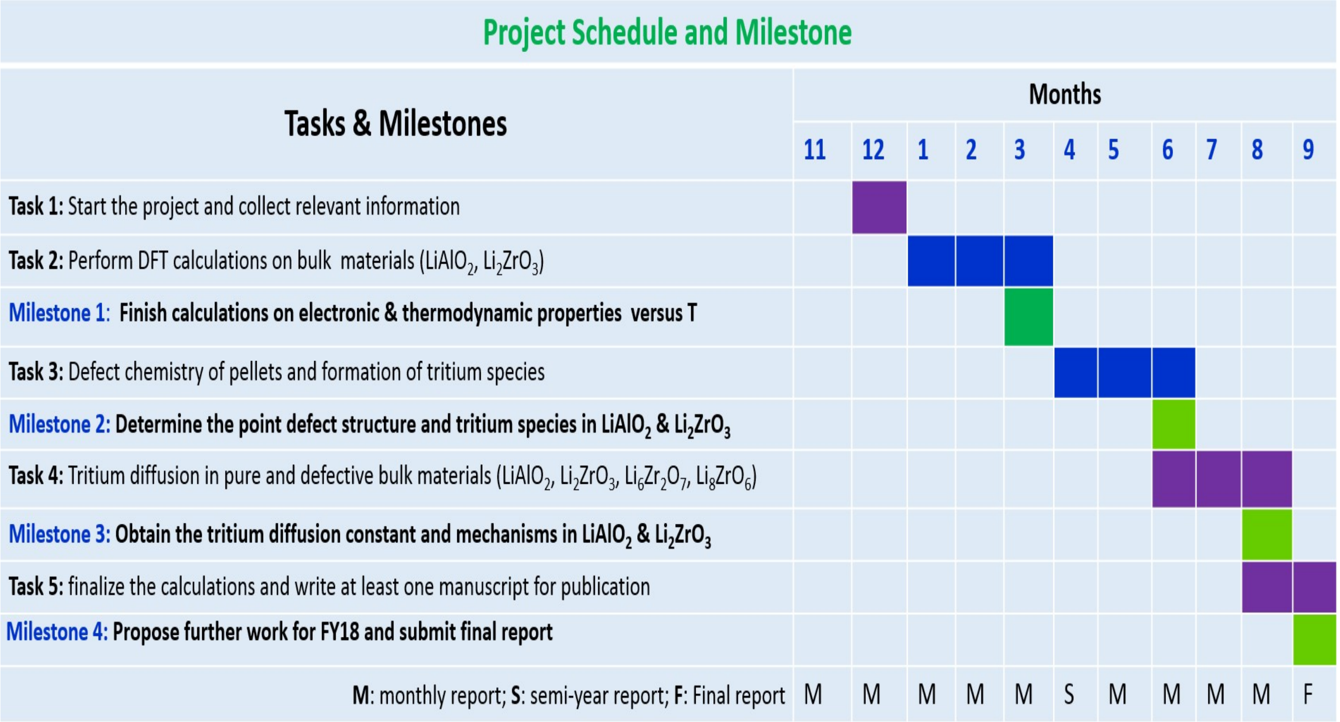

Project Schedule and Milestone

Tasks & Milestones	Months										
	11	12	1	2	3	4	5	6	7	8	9
Task 1: Start the project and collect relevant information		🟪									
Task 2: Perform DFT calculations on bulk materials ($LiAlO_2$, Li_2ZrO_3)			🟦	🟦	🟦						
Milestone 1: Finish calculations on electronic & thermodynamic properties versus T					🟩						
Task 3: Defect chemistry of pellets and formation of tritium species						🟦	🟦	🟦			
Milestone 2: Determine the point defect structure and tritium species in $LiAlO_2$ & Li_2ZrO_3								🟩			
Task 4: Tritium diffusion in pure and defective bulk materials ($LiAlO_2$, Li_2ZrO_3, $Li_6Zr_2O_7$, Li_8ZrO_6)								🟪	🟪	🟪	
Milestone 3: Obtain the tritium diffusion constant and mechanisms in $LiAlO_2$ & Li_2ZrO_3										🟩	
Task 5: finalize the calculations and write at least one manuscript for publication										🟪	🟪
Milestone 4: Propose further work for FY18 and submit final report											🟩
M: monthly report; **S**: semi-year report; **F**: Final report	M	M	M	M	M	S	M	M	M	M	F

1.3 Organization of Report

This report is organized as follow. In section 2, we present our results on the bulk properties of $LiAlO_2$ and lithium zirconates. Specifically, we provide the results for the density of states, band structure, phonon spectra, optical properties, and thermal conductivity calculations for the ^{7}Li and ^{6}Li isotopes of γ-$LiAlO_2$. In section 3 we analyze the solubility and defect chemistry of γ- $LiAlO_2$, Li_2ZrO_3 and Li_2TiO_3 systems. In the section 4, we describe the study of diffusion mechanisms of ^3_1T in these ceramics. Specifically, we calculated several possible pathways for substitutional, interstitial, and Li-T correlated diffusions. In addition to that, we calculated the energy barrier for diffusion of OT species. Finally, in the section 5, we conclude the report.

2. Bulk Properties of γ-$LiAlO_2$

2.1 Background

As an ultraslow lithium-ion conductor, lithium aluminate ($LiAlO_2$) has several potential applications. As coating for lithium-conducting electrodes and additive in composite electrolytes, it is widely used in battery industry.[1-6] As a membrane material, it is used for molten carbonate fuel cells.[7-9] In microelectronics, as a lattice matching substrate, the $LiAlO_2$ is used for epitaxial growth of II-V semiconductors (such as GaN, *etc.*) due to its excellent lattice mismatch to GaN (<1.4 % at <100>), its chemical stability at high temperature and as a cost effective replacement of ZnO. In addition, $LiAlO_2$ crystal can be used to replace ZnO and sapphire as an optical substrate. [10, 11]

In nuclear technology, due to its good thermo-physical and chemical stabilities at elevated temperatures and good tritium release characteristics, the $LiAlO_2$ is of interest as a solid tritium ($^{3}_{1}T$) breeder material for preparing tritium fuel for nuclear fusion.[12-19] In addition, this material can be used as a tritium-breeder material in fusion reactors. In tritium-producing burnable absorber rods (TPBARs), due to its high density, $LiAlO_2$ is used in the form of an annular ceramic pellet enriched with the ^{6}Li isotope and is located between the zircaloy-4 liner and nickel-plated zircaloy-4 tritium getter.[20-23] When irradiated in a pressurized water reactor (PWR), the ^{6}Li-enriched γ-$LiAlO_2$ pellets absorb neutrons, simulating the nuclear characteristics of a burnable absorber rod, and produce tritium through reaction $^{6}Li + n \rightarrow {}^{3}H + \alpha$.[24] The ^{3}H chemically reacts with the metal getter, which upon capture of the ^{3}H becomes a metal hydride. The defects and structural disorder may enhance the diffusion of Li within energy storage materials and breeders. However, the understanding of $^{3}_{1}T$ transport through the ceramic pellets and the barrier/cladding system is hampered by the lack of fundamental data such as hydrogen isotope solubility and diffusivity.[25-31] Therefore, it is essential to understand the effects of defect accumulation in γ-$LiAlO_2$ and how the Li transport changes as the structural disorder increases.

In the literature, there are several theoretical studies focusing on the electronic, structural and lattice dynamics properties of γ-$LiAlO_2$. Based on first-principles calculations, Wu *et al* investigated the electronic and elastic properties of γ-$LiAlO_2$ and obtained a 4.64 eV direct band gap. [32] Later, density functional perturbation theory approach was used by Ma *et al.* to investigate the dynamical and thermodynamic properties of γ-$LiAlO_2$.[33] A calculated band gap of 4.85 eV was obtained by this group which is larger than the previous reported value (4.64 eV) calculated by Wu *et al.* [32] The obtained thermodynamic properties (entropy, heat capacity, heat of formation, etc.) are in good agreement with the experimental data. Several theoretical investigations have been focused on the lithium/tritium diffusion in γ-$LiAlO_2$. Islam and Bredow explored the interstitial lithium diffusion pathway.[5] Wiedemann *et al* unraveled a ultraslow lithium-ion diffusion in γ-$LiAlO_2$.[34] Shah et al. explored the tritium defects in Li_2O which provided some guidelines for the case of γ-$LiAlO_2$.[35] Very recently, employing molecular dynamics simulations, Setyawan *et al.* explored the amorphization of γ-$LiAlO_2$ trying to identify the effect of the defects on the fast lithium ion transport in disordered ceramics created by neutron irradiation. [36]

In order to describe the tritium creation and diffusion in isotope ^{6}Li-enriched γ-$LiAlO_2$, in this study, we have performed extensive investigations on their structural, electronic, optical, lattice thermodynamic, and thermo-conductive properties. The obtained results provide a better understanding of bulk properties and are used as our starting point to further investigate their defect chemistry, tritium creation and diffusion in ^{6}Li-enriched γ-$LiAlO_2$.

2.2 Theoretical Method

The calculations performed in this work are based on first-principle density-functional theory (DFT) with plane-wave basis sets and the pseudopotential to describe the electron-ion interactions. The Vienna *Ab-initio* Simulation Package (VASP) [37-39] was employed in this study to calculate the electronic structures of the lithium zirconates and zirconia materials. In this study, all calculations have been done using the projector augmented wave (PAW) pseudo-potentials and the Perdew–Burke–Ernzerhof (PBE) exchange-correlation functional.[40, 41] Plane wave basis sets were used with a cutoff energy of 500 eV and a kinetic energy cutoff for augmentation charges of 605.4 eV. The k-point sampling grid of 8×8×8, obtained using the Monkhorst-Pack method,[42] were used for these bulk calculations. The valence electrons of all atoms contain the *s* and *p* orbitals. During the calculations, all atoms in the cell as well as the lattice dimensions and angles were relaxed to the equilibrium configurations. Since natural lithium contains about 3.75%~7.5% of ^{6}Li with the rest being ^{7}Li, the γ-$LiAlO_2$ used in TPBAR has been enriched the ^{6}Li concentration up to 25-30%.[24] To catch the effect of ^{6}Li isotope on its lattice dynamics and thermodynamic properties, in this study, we also conduct calculations on the γ-^{6}LiAlO$_2$ by substituting all ^{7}Li with ^{6}Li. When substituting the ^{7}Li with its ^{6}Li isotope, the pseudo-potential of ^{6}Li is obtained by modifying the mass in the standard ^{7}Li pseudo-potential. For band structure and phonon dispersion calculations, the symbols and coordinates of the high symmetrical points in the first Brillouin zone of the crystals are taken from Bradley and Cracknell's definitions.[43]

When considering the phase stability and transitions and the thermodynamics of crystalline materials, their fundamental properties are the phonon frequencies. The approaches of *ab initio* calculations fall into two classes: the linear response method,[44, 45] in which the dynamical matrix is expressed in terms of the inverse dielectric matrix describing the response of the valence electron density to a periodic lattice perturbation, and the direct method,[46-48] in which the forces are calculated via the Hellmann-Feynman theorem. Here, in this paper, we employ the PHONON software package[49] in which the direct method is applied following the formula derived by Parlinski *et al.*[48] to combine *ab initio* DFT with Phonon calculations. Following our previous approach,[50-52] the phonon dispersion and the thermodynamic properties (zero-point energy, free energy change and entropy change, *etc.*) can be carried out.

In the phonon calculations, a 2x2x2 supercell is created for γ-LiAlO$_2$ from its optimized unit cell that is calculated through DFT. The displacement of 0.03Å of non-equivalent atoms is generated. Then for the supercell, the DFT calculations were performed again to obtain the force on each atom due to the displacements. These forces are carried back to the PHONON package[49] to calculate the phonon dispersions and density of states. The partition function can be determined with the density of states. Knowing the partition function, the thermodynamic properties, such as internal energy, free energy, entropy, heat capacity, *etc*., can be evaluated at different temperatures.

Calculation of the lattice thermal conductivity has been done within the single-mode relaxation–time approximation based on first-principles anharmonic lattice dynamics calculations. For this purpose, we have used the methodology developed by Togo *et al*. as implemented in Phono3py code. [53] Within the relaxation time approximation, the lattice thermal conductivity tensor can be determined by solving the phonon Boltzmann equation as a sum of the form [53]

$$K_L = \frac{1}{NV_0}\sum_\lambda C_\lambda \boldsymbol{v}_\lambda \otimes \boldsymbol{v}_\lambda \tau_\lambda \tag{1}$$

where V_0 is the volume of the unit cell, $\boldsymbol{v}_\lambda$ and τ_λ are the group velocity and single mode relaxation time of the phonon mode λ, C_λ is the mode dependent heat capacity and N is the total number of q points used for sampling of the Brillouin zone. Calculations of these mode-dependent quantities have been done using second- and third-order force constants which were obtained using finite atomic displacements within periodic supercell models.

In this case, optimization of the crystal structure and evaluation of the corresponding energies and forces have been done using plane-wave density functional theory calculations based on VASP [37-39]. In addition to PBE, the PBEsol [54] functional has also been used to describe exchange-correlation effects together with the projector augment wave (PAW) method of Blöchl [41] in the implementation of Kresse and Joubert.[55] As demonstrated by Skelton et al.[56] this functional shows good general performance to reproduce the temperature dependence of material properties including phonon related properties. All calculations were done using a cutoff energy of 900 eV and an 8x8x8 Monkhorst-Pack [42] grid was used for optimization of the unit cell. These computational conditions allow convergence of the total energy to within 1 meV/atom and of the pressure to within 1 kbar. Optimization of crystallographic unit cell parameters lead to values of 5.1713, 5.1713, and 6.2615 Å which differ by only 0.05, 0.05 and -0.10 % relative to corresponding experimental neutron diffraction data.[57] In calculation of the force constants the total energies were minimized using a convergence threshold of 10^{-8} eV. Nonanalytical term correction [58] was also included using the Born effective charges calculated based on density functional perturbation theory. For the third order force constants, 2x2x2 supercells containing 128 atoms were used having their reciprocal spaces sampled using 4x4x4 k-point grids. Upon considering symmetry a total number of 9230 displacements were evaluated in this case. In calculation of the thermal conductivity the tetrahedron method was used using 21x21x21 integration meshes. Additional convergence tests were done by increasing the integration meshes to 31x31x31.

To study the optical properties, the frequency-dependent dielectric matrix in the long wavelength limit (q→0) can be calculated using the sum over states approach.[59-61] The formula for the imaginary part of the dielectric constant is a 3x3 Cartesian tensor

$$\varepsilon_2^{\alpha\beta}(\omega) = \frac{4\pi^2 e^2}{\Omega} \lim_{q\to 0} \frac{1}{q^2} \sum\nolimits_{c,v,k} 2\omega_k\, \delta(\epsilon_{ck} - \epsilon_{vk} - \omega) \times < u_{ck+e_\alpha q} \left| u_{vk} >< u_{ck+e_\beta q} \right| u_{vk} >^* \tag{2}$$

where the indices *c* and υ correspond to the conduction and valence band states, respectively and $u_{c\kappa}$ is the periodic part of the orbitals at the k-point κ. The vector $\mathbf{e}_\alpha$ are unit vectors for the three Cartesian directions.[60, 61] The real part of the dielectric constant tensor can be derived from the imaginary part using Kramers-Kronig relations:

$$\varepsilon_1^{\alpha\beta}(\omega) = 1 + \frac{2}{\pi} P \int_0^\infty \frac{\varepsilon_2^{\alpha\beta}(\omega')\omega'}{\omega'^2 - \omega^2} d\omega' \tag{3}$$

where P denotes the principle value, the values of α and β are 1 to 3. The real part of the optical conductivity (σ(ω)) is defined as

$$\sigma_1(\omega) = Re[\sigma(\omega)] = \frac{\varepsilon_2(\omega)\cdot\omega}{60} \tag{4}$$

where σ(ω) and ω are in the SI unit of Siemens/cm and cm^{-1} respectively. The corresponding imaginary part of σ(ω) in SI unit is [62]

$$\sigma_2(\omega) = -\frac{\omega(\varepsilon_1(\omega) - 1)}{60} \tag{5}$$

The complex dielectric constant can be expressed as:[63]

$$\varepsilon(\omega) = \varepsilon_1(\omega) + i\varepsilon_2(\omega) = \frac{4\pi i}{\omega}\sigma(\omega) = (\tilde{n} + i\tilde{k})^2 \tag{6}$$

where $\tilde{n}$ and $\tilde{k}$ are the index of refraction and the extinction coefficient respectively, and can be evaluated by the calculated dielectric constants as

$$\tilde{n} = \frac{1}{\sqrt{2}}(\varepsilon_1 + (\varepsilon_1^2 + \varepsilon_2^2)^{\frac{1}{2}})^{\frac{1}{2}} \tag{7}$$

$$\tilde{\kappa} = \frac{1}{\sqrt{2}}(-\varepsilon_1 + (\varepsilon_1^2 + \varepsilon_2^2)^{\frac{1}{2}})^{\frac{1}{2}} \tag{8}$$

In the case of normal incidence, the reflectivity R and the absorption coefficient α in terms of $\tilde{n}$ and $\tilde{k}$ are defined as

$$R = \frac{(\tilde{n}-1)^2 + \tilde{k}}{(\tilde{n}+1)^2 + \tilde{k}} \tag{9}$$

$$\alpha = 4\pi\omega\tilde{k} \tag{10}$$

In SI unit, ω and α are given in cm^{-1}. In all the cases, both the low frequency region $\omega\tau \ll 1$ (τ is the relaxation time) and the high frequency region $\omega\tau \gg 1$ are extensively studied to analyze the exact ground state of the material as these two regions carry the signatures of two distinct conduction mechanisms within a solid. While the low frequency region is dominated by free carriers which are in abundance in a metal, the high frequency region is dominated by inter-band electronic transitions typical of a dielectric material.

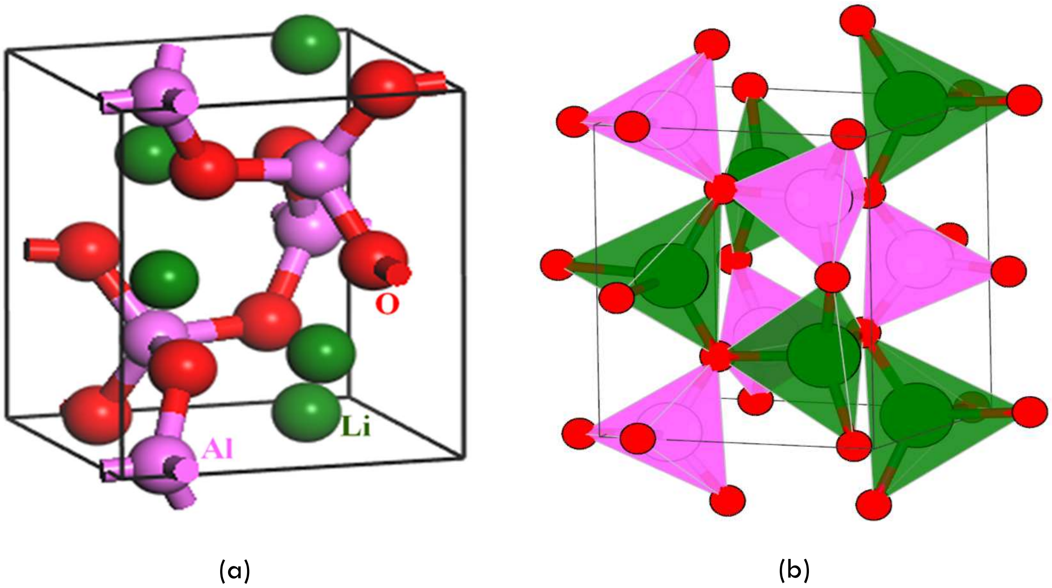

Figure 1 The crystal structures of γ-$LiAlO_2$ with space group $P4_12_12$ (#92). (a) unit cell; (b) the distorted [AlO_4] and [LiO_4] tetrahedra form three-dimensional network connecting through O atom. Atom types are indicated in (a).

2.3 Results and Discussion

2.3.1 Structural and electronic properties

So far six polymorphs of $LiAlO_2$ have been reported:[34] hexagonal α- ($R\bar{3}m$, $NaCrS_2$ type), orthorhombic β- ($Pna2_1$, β-$NaFeO_2$ type), tetragonal γ-($P4_12_12$/$P4_32_12$, γ-$LiAlO_2$ type), tetragonal δ- ($I4_1/amd$, α-$LiFeO_2$ type), cubic ε-$LiAlO_2$ ($I4_132$, structure unknown), and a debatable monoclinic phase ($P_{2/m}$, structure unknown). Being the most stable form under ambient conditions, γ-$LiAlO_2$ was fully characterized using powder neutron and single-crystal X-ray techniques.[64] Figure 1 shows the crystal structure of γ-$LiAlO_2$. As one can see from Figure 1(b) that in γ-$LiAlO_2$, distorted MO_4 tetrahedra (M = Al, Li) form a three-dimensional network. Each tetrahedron shares one edge with a tetrahedron containing a different kind of metal ion. In these pairs, each vertex is shared with two additional tetrahedra, one of each kind. The optimized crystal constants and coordinates are summarized in Table 2.1.

Table 2.1 The experimental and optimized crystal structural constants of γ-$LiAlO_2$ and its ^{6}Li isotope substitution.

Crystal & space group	Lattice constants		Fractional coordinates	
	experimental	optimized	experimental	optimized
γ-$LiAlO_2$ $P4_12_12$(No.92) [a] Z=4	a=5.1685Å c=6.2565Å V=167.132 Å^3	a=5.224864Å c=6.312813Å V=172.3347 Å^3	Li: (0.8096, 0.8086, 0.0000) Al: (0.1761, 0.1761, 0.0000) O: (0.3376, 0.2901, 0.7726)	Li: (0.813722, 0.813722, 0.000000) Al: (0.176456, 0.176456, 0.000000) O: (0.337480, 0.291242, 0.772071)
γ-$^6LiAlO_2$		a=5.226231Å c=6.313303Å V=172.4384 Å^3		Li: (0.813732, 0.813732, 0.000000) Al: (0.176479, 0.176479, 0.000000) O: (0.337560, 0.291222, 0.772098)

[a] Experimental data from ref.[64]

Figure 2(a) shows the calculated band structure of γ-$LiAlO_2$. The corresponding total density of states (TDOS) and the partial density of states (PDOS) for each element are shown in Figure 2(b). As one can see the calculated band gap is 4.64 eV which is close to the other calculated values of 4.85 eV[33] and 4.64 eV[32], but is much lower than the experimental estimated value of 6.5 eV[59]. Due to the DFT approximations, which underestimate the excited state energies, the calculated band gaps of solids and are smaller than their experimental measurements. Such discrepancy is reasonable as γ-$LiAlO_2$ is a wide band-gap material. From the Figure 2(b), one can see that the 1st valence band (VB) just below the Fermi energy is mainly formed by *p* orbitals of Li, O and Al. The *s* orbital of Al also contributes to the lower portion of the 1st VB. The 2nd VB is mainly formed by *s* orbital of O, *p*, *s* orbitals of Li and Al. The conduction band (CB) is mainly contributed by *s* and *p* orbitals of Al and Li. The band widths are summarized in Table 2.2.

The cohesive energy (E_C) is calculated by subtracting the total bulk energy (E_{DFT} in Table 2.2) from the sum of total energies of the related atoms (such as O_2, Li and Al metals) using the same level calculations (in our case, we get E_{Li_metal}= -1.45690eV, E_{Al_metal}= -3.67219eV, and E_{O2}= -8.74410eV). The calculated E_C as well as other values from references are also listed in Table 2.2.

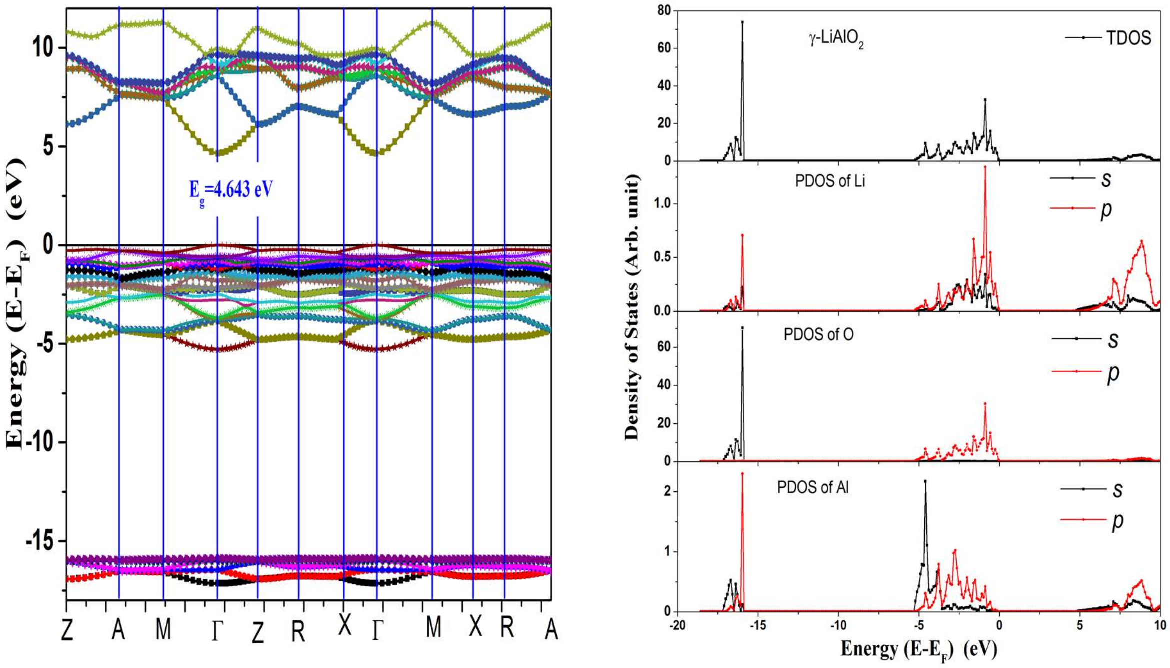

(a)

(b)

Figure 2 The calculated electronic properties of γ-$LiAlO_2$: (a) band structure, (b) total and atomic partial density of states.

Table 2.2 The calculated band gaps and valence band (VB) widths of γ-$LiAlO_2$ and its corresponding zero-point energies (E_{zp}), and the entropies at T=298 K from phonon calculations

Crystal	E_{DFT} (eV/cell)	Cohesive energy E_c (eV)	2nd VB width (eV)	Gap between 1st VB & 2nd VB (eV)	1st VB width (eV)	Band Gap (eV)	E_{zp} (kJ/mol)	Entropy (J/mol.K)
γ-$LiAlO_2$	-26.32911	12.45592	1.243	10.666	5.230	4.763, 4.64[a],4.85[b]	32.354	54.963
γ-$^6LiAlO_2$	-26.33094	12.45775					32.875	53.672

[a] Ref. [32]

[b] Ref. [33]

Since the difference between ^{6}Li and ^{7}Li isotopes is their masses, substituting ^{7}Li with ^{6}Li in γ-$LiAlO_2$ does not alter its electronic property. That means the γ-$^6LiAlO_2$ possesses same electronic structure as γ-$LiAlO_2$. However, their lattice dynamics and optical properties are different as discussed in the following sections.

2.3.2 Lattice phonon dynamics, thermodynamic properties

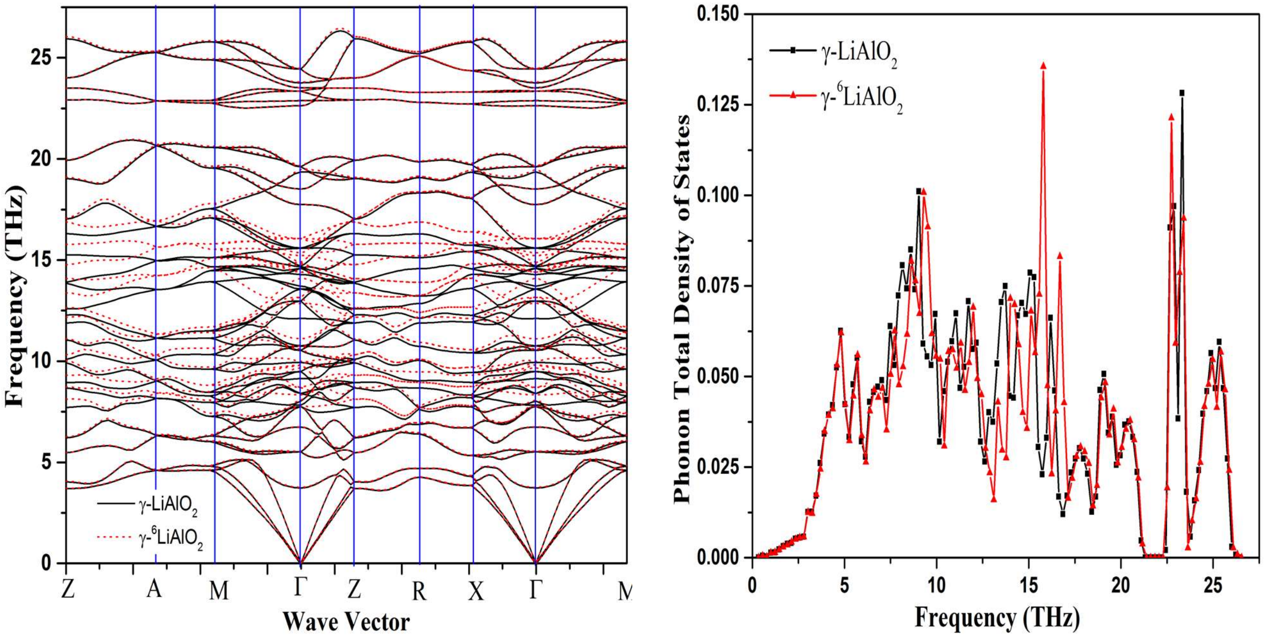

(a) (b)

Figure 3 The calculated lattice phonon dynamical properties of γ-$LiAlO_2$ and its ^{6}Li isotope substitution: (a) phonon dispersions; (b) phonon density of states.

In γ-$LiAlO_2$ unit cell, there are four formula units (Z=4). Hence, there are 48 vibrational modes. Its corresponding point group is D4 and its irreducible representations is 11E(IR) + $5A_1$(R) + $7A_2$(I) + $7B_1$(R) + $5B_2$(R). Among them, 7 vibrational modes are Infrared (IR) active, 17 modes are Raman (R) active, and 22 vibrational modes in double states E are both IR and Raman active. The phonon dispersions of γ-$LiAlO_2$ and ^{6}Li isotope substituted γ-$^6LiAlO_2$ are shown in Figure 3(a) and their corresponding total phonon density of states are shown in Figure 3(b). As one can see that along the wave-vectors no obviously soft mode (with negative frequency) was found. This indicates that the γ-$LiAlO_2$ and ^{6}Li isotope substituted γ-$^6LiAlO_2$ are thermodynamically stable. Since the lattice dynamics frequencies are mass dependent, the phonon dispersion of γ-$^6LiAlO_2$ is different from γ-$LiAlO_2$, particularly in the frequency range of 10-20 THz as shown in Figure 3. Obviously, such differences will affect their thermodynamic properties, although the magnitude of the effect may not be very large given the good agreement of the phonon densities of states in Figure 3b.

Figure 4 shows the calculated phonon free energies and entropies of γ-$LiAlO_2$ and ^{6}Li isotope substituted γ-^{6}LiAlO$_2$. One can see that by increasing the temperature from 0 K up to 1500 K, their phonon free energies are decreased while their entropies are increased. The free energy and entropy differences between of γ-LiAlO$_2$ and ^{6}Li isotope substituted γ-^{6}LiAlO$_2$ are relatively small along the entire temperature range. The free energy G(T) can be approximately evaluated by adding the DFT energy (in Table 2.2) with phonon free energy (Figure 4(a)). To obtain its thermodynamic properties (such as Gibbs free energy change ΔG(T), enthalpy change ΔH(T), *etc*.), a reference state is needed.

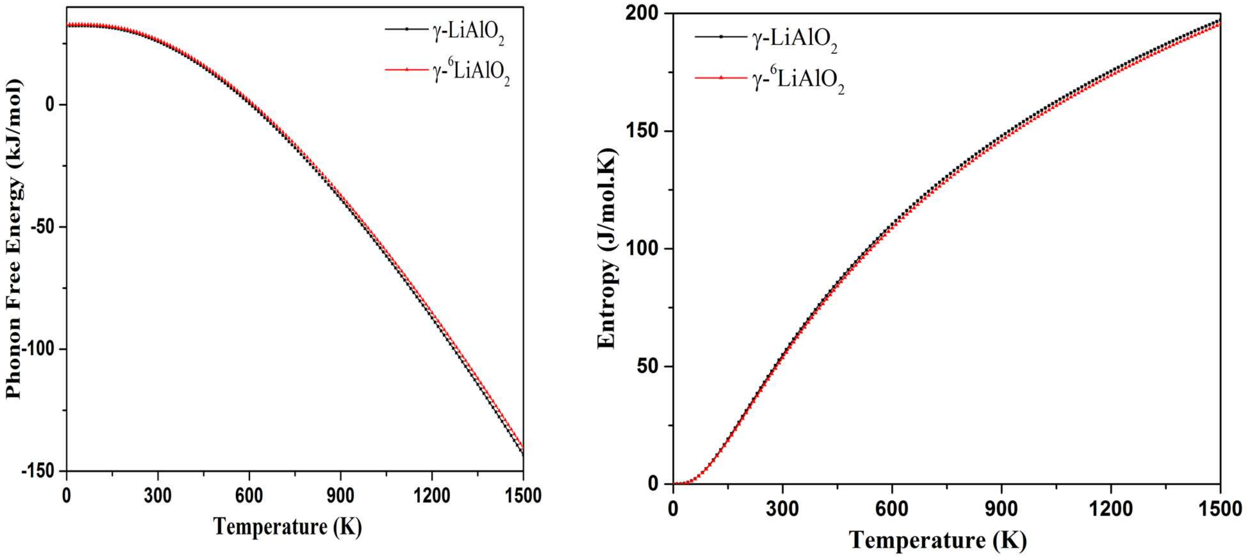

(a)

(b)

Figure 4 The calculated the thermodynamic properties of γ-LiAlO$_2$ and its ^{6}Li isotope substitution: (a) phonon free energy; (b) entropy.

2.3.3 Thermal conductivity

The variation with temperature of the calculated lattice thermal conductivity of γ -LiAlO$_2$ is presented in Figure 5 together with the corresponding available experimental data. As seen from this Figure there are noticeable differences among the two sets of experimental data which were measured on samples of different porosities. It has been argued [65] that the difference among the two sets of thermal conductivities is due to the widely different chemical processes used in preparation, which can lead to different porosity, pore morphology and grain size, as well as the approach used in measuring the specific heat of γ -LiAlO$_2$.

The conclusions drawn from Figure 5 are that the PBEsol results are a significantly better representation of the experimental curves than the PBE results, and that they are in much better agreement with the experimental data obtained by Hollenberg and Baker [66]. At 300K, the calculated thermal conductivity is within a factor of 1.4 from the corresponding data obtained by this group. Calculations also show a small anisotropy in thermal conductivity along (*a* or *b*) crystallographic directions relative to *c* direction.

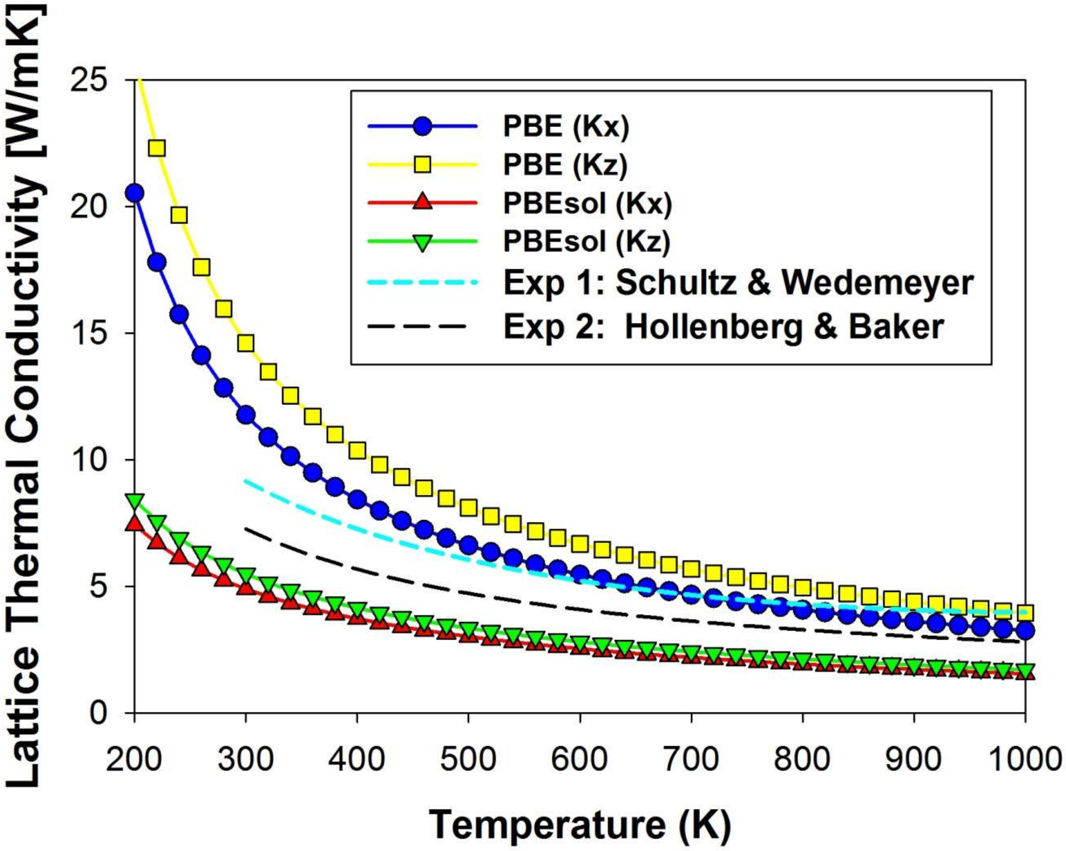

Figure 5 Variation with temperature of the lattice thermal conductivity for γ -$LiAlO_2$. For calculated values the individual components along *a* axis (Kx)and *c* axis (Kz) are given. For comparison the experimental data from Exp.1 [65] and Exp. 2 [66] are also included.

2.3.4 Optical properties

Figure 6 shows the calculated dielectric matrix of γ-$LiAlO_2$ and ^6Li isotope substituted γ-$^6LiAlO_2$. Obviously, due to the high symmetrical and isotropic features of the crystals, the off-diagonal elements of their dielectric tensors are zero. Along the principle axes *x* and *y*, they have equal values of real part, ε_1(or ε’), and imaginary part, ε_2(or ε”) while along principle axis *z* the ε_1 and ε_2 have different values along the energy. Corresponding conversions to frequency or wave-length units can be obtained using the conversion factors of 1eV = 241.797 GHz = 8065.48 cm^{-1}. Different from their lattice thermodynamic properties, the dielectric matrix of γ-LiAlO$_2$ and ^{6}Li isotope substituted γ-^{6}LiAlO$_2$ are same, because their ε” and ε’ matrix only depend on their electronic structures as defined in Eqs. (2) and (3). At zero frequency, the imaginary dielectric matrix (ε”) is zero while the real part components (ε’) have finite values (2.3) due to their wide band-gap.

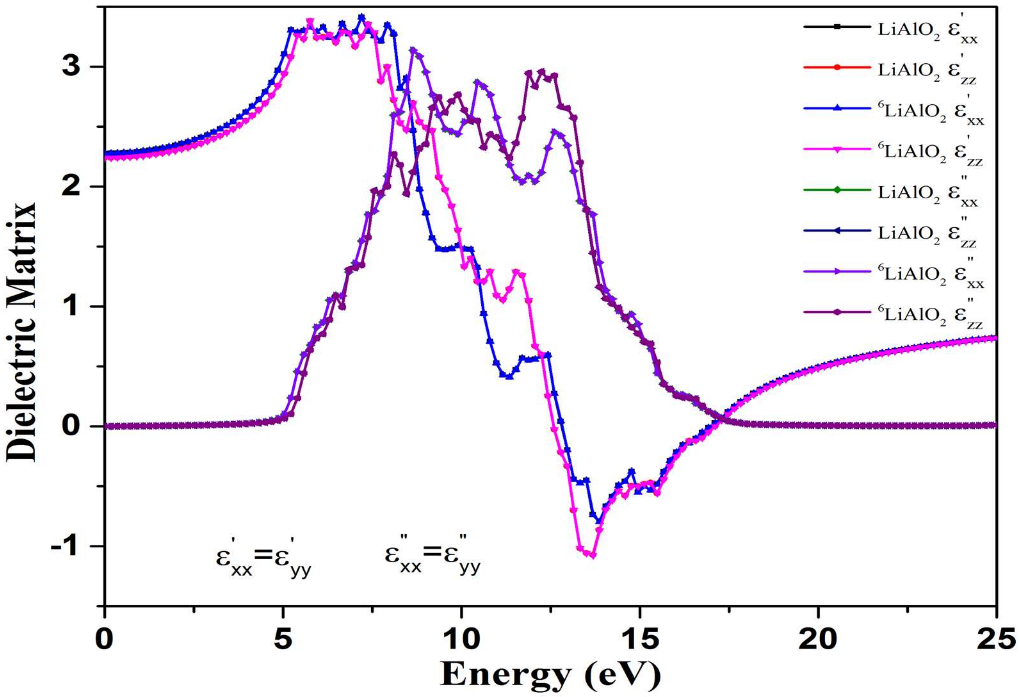

Figure 6 The calculated the dielectric matrix of γ-LiAlO$_2$ and its ^{6}Li isotope substitution.

Based on the calculated dielectric matrix of γ-LiAlO$_2$ and ^{6}Li isotope substituted γ-^{6}LiAlO$_2$ shown in Figure 6 and by following the equations (2)-(10), their index of refraction ($\tilde{n}$), extinction coefficient ($\tilde{k}$), reflectivity (R), absorption coefficient (α), and the conductivity (σ) can be obtained. Figure 7 shows the calculated $\tilde{n}$, $\tilde{k}$, α and σ of γ-LiAlO$_2$ versus wavelength (nm). Obviously, these optical properties are identical for γ-LiAlO$_2$ and ^{6}Li isotope substituted γ-^{6}LiAlO$_2$.

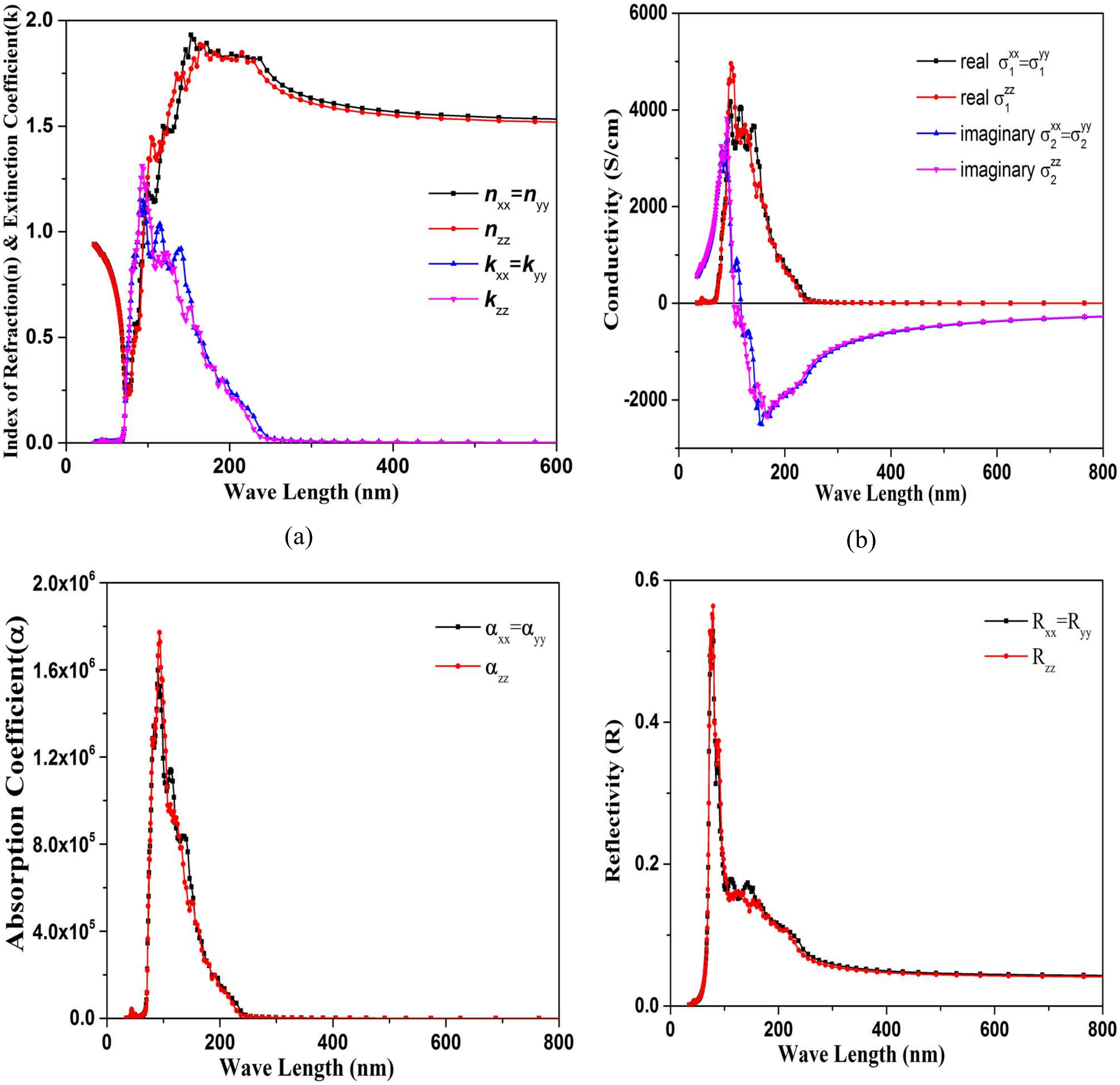

(a)

(b)

(c)

(d)

Figure 7 The calculated optical properties of γ-$LiAlO_2$ and its ^6Li isotope substitution: (a) index of refraction (n) and extinction coefficient (k), (b) conductivity (σ) (c) adsorption coefficient (α), (d) reflectivity (R).

For applications as optical sensor materials in conjunction with the optical fiber platform, the most interested wavelength range is from ultraviolet (UV) (10-400 nm) through the visible spectrum (400-800 nm) to Near Infrared and Infrared (IR) (>800 nm), particularly, around the visible and near infrared range (~400-2,000 nm). At very low-energy (high wavelength) range, the optical conductivity results from the free carrier response. As one can see from Figure 7(b) that at high wavelength range (>300 nm) the optical conductivity is close to zero, which means the free carrier response in γ-$LiAlO_2$ is very small because it has a large band gap as shown in Figure 2. Within 50nm-300nm, the optical conductivity has a set of peaks which result from electron hopping among VB-CB gaps. With VB-CB hopping, large absorption coefficient and reflectivity can be observed as shown in Figure 7(c) and (d). Obviously, the electron hopping between VB and CB plays a dominant role in γ-$LiAlO_2$ optical properties.

2.4 Summary

In this study, by combining density functional theory and lattice phonon dynamics approach, the electronic, optical, thermal conductivity, and thermodynamic properties of γ-$LiAlO_2$ and ^{6}Li isotope substituted γ-$^6LiAlO_2$ have been investigated. The obtained results showed that γ-$LiAlO_2$ possesses a wide band-gap of 4.64 eV. The valence band is mainly formed by *p* orbitals of Li, O, and Al. Substituting ^{7}Li with ^{6}Li isotope in γ-$LiAlO_2$ do not alter their electronic structures and optical properties.

When substituting ^{7}Li with ^{6}Li isotope in γ-$LiAlO_2$ the lattice phonon frequencies have obviously change, particularly in the range of 5-15THz out of entire frequency spectra (0-26 THz). By taking into account the anharmonic effects into the phonon calculations, the lattice thermal conductivity of γ-$LiAlO_2$ was obtained and it was found to be in good agreement over a wide range of temperatures with the available experimental data. By increasing temperature from 0 K up to 1500 K, the phonon free energies for both γ-$LiAlO_2$ and ^{6}Li isotope substituted γ-$^6LiAlO_2$ are decreased while their entropies are increased. The optical conductivity at low wavelengths (50-300 nm) is due to VB-CB hopping.

2.5 References

[1] H. Cao, B.J. Xia, Y. Zhang, N.X. Xu, $LiAlO_2$-coated $LiCoO_2$ as cathode material for lithium ion batteries, Solid State Ionics, 176 (2005) 911-914.

[2] L.J. Li, Z.Y. Chen, Q.B. Zhang, M. Xu, X. Zhou, H.L. Zhu, K.L. Zhang, A hydrolysis-hydrothermal route for the synthesis of ultrathin $LiAlO_2$-inlaid $LiNi_{0.5}Co_{0.2}Mn_{0.3}O_2$ as a high-performance cathode material for lithium ion batteries, J Mater Chem A, 3 (2015) 894-904.

[3] M.A.K.L. Dissanayake, Nano-composite solid polymer electrolytes for solid state ionic devices, Ionics, 10 (2004) 221-225.

[4] S. Indris, P. Heitjans, R. Uecker, B. Roling, Li Ion Dynamics in a $LiAlO_2$ Single Crystal Studied by Li-7 NMR Spectroscopy and Conductivity Measurements, J Phys Chem C, 116 (2012) 14243-14247.

[5] M.M. Islam, T. Bredow, Interstitial Lithium Diffusion Pathways in gamma-$LiAlO_2$: A Computational Study, J Phys Chem Lett, 6 (2015) 4622-4626.

[6] L.F. Hu, Z.L. Tang, Z.T. Zhang, New composite polymer electrolyte comprising mesoporous lithium aluminate nanosheets and PEO/$LiClO_4$, J Power Sources, 166 (2007) 226-232.

[7] H. Takahashi, N. Yamazaki, T. Watanabe, K. Suzuki, Gamma lithium aluminate product and process of making., in: N.C.I. Co. (Ed.), 2001, pp. US-6,290,928.

[8] D. Wohlmuth, V. Epp, P. Bottke, I. Hanzu, B. Bitschnau, I. Letofsky-Papst, M. Kriechbaum, H. Amenitsch, F. Hofer, M. Wilkening, Order vs. disorder-a huge increase in ionic conductivity of nanocrystalline $LiAlO_2$ embedded in an amorphous-like matrix of lithium aluminate, J Mater Chem A, 2 (2014) 20295-20306.

[9] S. Terada, I. Nagashima, K. Higaki, Y. Ito, Stability of $LiAlO_2$ as electrolyte matrix for molten carbonate fuel cells, J Power Sources, 75 (1998) 223-229.

[10] S.K. Duan, X.G. Teng, P.D. Han, D.C. Lu, Growth and characterization of GaN on $LiGaO_2$ and $LiAlO_2$, in: K. Onabe, K. Hiramatsu, K. Itaya, Y. Nakano (Eds.) 2nd International synposium on Blue Laser and Light Emitting Diodes OHMSHA LTD, CHIBA, JAPAN 1998, pp. 158-161.

[11] K. Xu, J. Xu, P.Z. Deng, Y.Z. Zhou, G.Q. Zhou, R.S. Qiu, Z.J. Fang, gamma-$LiAlO_2$ single crystal: a novel substrate for GaN epitaxy, J Cryst Growth, 193 (1998) 127-132.

[12] B. Rasneur, Tritium Breeding Material - Gamma-$LiAlO_2$, Fusion Technol, 8 (1985) 1909-1914.

[13] M. Ubeyli, Impact of solid breeder materials on tritium breeding in a hybrid reactor, J Fusion Energ, 25 (2006) 99-106.

[14] M. Nishikawa, A. Baba, Y. Kawamura, Tritium inventory in a $LiAlO_2$ blanket, J Nucl Mater, 246 (1997) 1-8.

[15] M. Caorlin, G. Gervasini, F. Reiter, The impact of tritium solubility and diffusivity on inventory and permeation in liquid breeder blankets Fusion Technol, 14 (1988) 663-670.

[16] Y. Kawamura, T. Yamanishi, Tritium recovery from blanket sweep gas via ceramic proton conductor membrane, Fusion Eng Des, 86 (2011) 2160-2163.

[17] M. Nishikawa, A. Baba, Tritium inventory in Li_2ZrO_3 blanket, J Nucl Mater, 257 (1998) 162-171.

[18] N.B. Morley, M.A. Abdou, M. Anderson, P. Calderoni, R.J. Kurtz, R. Nygren, R. Raffray, M. Sawan, P. Sharpe, S. Smolentsev, S. Willms, A.Y. Ying, Overview of fusion nuclear technology in the US, Fusion Eng Des, 81 (2006) 33-43.

[19] Y.Y. Liu, M.C. Billone, A.K. Fischer, S.W. Tam, R.G. Clemmer, G.W. Hollenberg, Solid Tritium Breeder Materials Li_2O and $LiAlO_2$ - a Data-Base Review, Fusion Sci Technol, 8 (1985) 1970-1984.

[20] J. Lyons, E. Love, K. Burns, TEACUP: A Tritium Management and Supplemental Core Follow Program, Fusion Sci Technol, 71 (2017) 616-621.

[21] W.L. Jiang, J.D. Zhang, L. Kovarik, Z.H. Zhu, L. Price, J. Gigax, E. Castanon, X.M. Wang, L. Shao, D.J. Senor, Irradiation effects and hydrogen behavior in HI and He implanted gamma-$LiAlO_2$ single crystals, J Nucl Mater, 484 (2017) 374-381.

[22] K.A. Burns, E.F. Love, C.K. Thornhill, Description of the Tritium-Producing Burnable Absorber Rod for the Commercial Light Water Reactor, TTQP-1-015, Revision 19, PNNL, 2012.

[23] W.L. Jiang, J. Zhang, D.J. Edwards, N.R. Overman, Z. Zhu, L. Price, J. Gigax, E. Castanon, L. Shao, D.J. Senor, Nanostructural evolution and behavior of H and Li in ion-implanted gamma-$LiAlO_2$, J Nucl Mater, 494 (2017) 411-421.

[24] D.J. Senor, Recommendations for Tritium Science and Technology Research and Development in Support of the Tritium Readiness Campaign, TTP-7-084, PNNL, 2014.

[25] K. Okuno, H. Kudo, Diffusion-Controlled Tritium Release from Neutron-Irradiated Gamma-$LiAlO_2$, J Nucl Mater, 138 (1986) 210-214.

[26] K. Okuno, H. Kudo, Tritium diffusivity in lithium-based ceramic breeders irradiated with neutrons, Fusion Eng Des, 8 (1989) 355-358.

[27] F. Ono, S. Tanaka, M. Yamawaki, Tritium sorption by cement and subsequent release, Fusion Eng Des, 28 (1995) 378-385.

[28] A. Badawi, A.R. Raffray, M.A. Abdou, Analysis of Tritium Release from $LiAlO_2$ in the Tequila Experiment, Using the Mistral Code, Fusion Eng Des, 17 (1991) 73-78.

[29] L.M. Carrera, J. Jimenez-Becerril, R. Basurto, J. Arenas, B.E. Lopez, S. Bulbulian, P. Bosch, Tritium recovery from nanostructured $LiAlO_2$, J Nucl Mater, 299 (2001) 242-249.

[30] M. Nishikawa, T. Kinjyo, T. Ishizaka, S. Beloglazov, T. Takeishi, M. Enoeda, T. Tanifuji, Release behavior of bred tritium from $LiAlO_2$, J Nucl Mater, 335 (2004) 70-76.

[31] M. Oyaidzu, T. Takeda, H. Kimura, A. Yoshikawa, M. Okada, K. Munakata, M. Nishikawa, K. Okuno, Correlation between annihilation of radiation defects and tritium release in neutron-irradiated $LiAlO_2$, Fusion Sci Technol, 48 (2005) 638-641.

[32] S.Q. Wu, Z.F. Hou, Z.Z. Zhu, First-principles study on the structural, elastic, and electronic properties of gamma-$LiAlO_2$, Comp Mater Sci, 46 (2009) 221-224.

[33] S.G. Ma, Y.H. Shen, T. Gao, P.H. Chen, First-principles calculation of the structural, electronic, dynamical and thermodynamic properties of gamma-$LiAlO_2$, Int J Hydrogen Energ, 40 (2015) 3762-3770.

[34] D. Wiedemann, S. Nakhal, J. Rahn, E. Witt, M.M. Islam, S. Zander, P. Heitjans, H. Schmidt, T. Bredow, M. Wilkening, M. Lerch, Unravelling Ultraslow Lithium-Ion Diffusion in gamma-$LiAlO_2$: Experiments with Tracers, Neutrons, and Charge Carriers, Chem Mater, 28 (2016) 915-924.

[35] R. Shah, A. Devita, M.C. Payne, Ab-Initio Study of Tritium Defects in Lithium-Oxide, J Phys-Condens Mat, 7 (1995) 6981-6992.

[36] W. Setyawan, D.J. Senor, R. Devanathan, Insights on Amorphization of Lithium Aluminate from Atomistic Simulation, J Phys Chem C, 121 (2017) 7635-7642.

[37] G. Kresse, J. Hafner, Abinitio Molecular-Dynamics for Liquid-Metals, Phys. Rev. B, 47 (1993) 558-561.

[38] G. Kresse, J. Furthmuller, Efficient iterative schemes for *ab initio* total-energy calculations using a plane-wave basis set, Phys. Rev. B, 54 (1996) 11169-11186.

[39] G. Kresse, J. Furthmuller, Efficiency of *ab-initio* total energy calculations for metals and semiconductors using a plane-wave basis set, Comp Mater Sci, 6 (1996) 15-50.

[40] J.P. Perdew, K. Burke, M. Ernzerhof, Generalized gradient approximation made simple, Physical Review Letters, 77 (1996) 3865-3868.

[41] P.E. Blochl, Projector Augmented-Wave Method, Phys Rev B, 50 (1994) 17953-17979.

[42] H.J. Monkhorst, J.D. Pack, Special Points for Brillouin-Zone Integrations, Phys. Rev. B, 13 (1976) 5188-5192.

[43] C.J. Bradley, A.P. Cracknell, The mathematical theory of symmetry in solids, Clarendon press, Oxford, 1972.

[44] S. Baroni, P. Giannozzi, A. Testa, Elastic-Constants of Crystals from Linear-Response Theory, Physical Review Letters, 59 (1987) 2662-2665.

[45] S. Baroni, S. de Gironcoli, A. Dal Corso, P. Giannozzi, Phonons and related crystal properties from density-functional perturbation theory, Rev Mod Phys, 73 (2001) 515-562.

[46] W. Frank, C. Elsasser, M. Fahnle, Ab-Initio Force-Constant Method for Phonon Dispersions in Alkali-Metals, Physical Review Letters, 74 (1995) 1791-1794.

[47] K. Kunc, R.M. Martin, Abinitio Force-Constants of Gaas - a New Approach to Calculation of Phonons and Dielectric-Properties, Physical Review Letters, 48 (1982) 406-409.

[48] K. Parlinski, Z.Q. Li, Y. Kawazoe, First-principles determination of the soft mode in cubic ZrO_2, Physical Review Letters, 78 (1997) 4063-4066.

[49] K. Parlinski, Software PHONON, DOI (2006).

[50] Y. Duan, J. Lekse, X. Wang, B. Li, B. Alcantar-Vazquez, H. Pfeiffer, J.W. Halley, Electronic Structure, Phonon Dynamical Properties, and Capture Capability of $Na_{2-x}M_xZrO_3$ (M=Li,K): Density-Functional Calculations and Experimental Validations, Physical Review Applied, 3 (2015) 044013.

[51] Y. Duan, K. Parlinski, Density functional theory study of the structural, electronic, lattice dynamical, and thermodynamic properties of Li_4SiO_4 and its capability for CO_2 capture, Phys Rev B, 84 (2011) 104113.

[52] Y. Duan, Electronic structural and electrochemical properties of lithium zirconates and their capabilities of CO_2 capture: A first-principles density-functional theory and phonon dynamics approach, J Renew Sustain Ener, 3 (2011) 013102.

[53] A. Togo, L. Chaput, I. Tanaka, Distributions of phonon lifetimes in Brillouin zones, Phys Rev B, 91 (2015) 094306.

[54] J.P. Perdew, A. Ruzsinszky, G.I. Csonka, O.A. Vydrov, G.E. Scuseria, L.A. Constantin, X.L. Zhou, K. Burke, Restoring the density-gradient expansion for exchange in solids and surfaces, Physical Review Letters, 100 (2008) 136406.

[55] G. Kresse, D. Joubert, From ultrasoft pseudopotentials to the projector augmented-wave method, Phys Rev B, 59 (1999) 1758-1775.

[56] J.M. Skelton, D. Tiana, S.C. Parker, A. Togo, I. Tanaka, A. Walsh, Influence of the exchange-correlation functional on the quasi-harmonic lattice dynamics of II-VI semiconductors, Journal of Chemical Physics, 143 (2015) 064710.

[57] M. Marezio, Crystal Structure and Anomalous Dispersion of Gamma-$LiAlO_2$, Acta Crystallogr, 19 (1965) 396-400.

[58] R.M. Pick, M.H. Cohen, R.M. Martin, Microscopic Theory of Force Constants in Adiabatic Approximation, Phys Rev B-Solid St, 1 (1970) 910-920.

[59] M. Gajdos, K. Hummer, G. Kresse, J. Furthmuller, F. Bechstedt, Linear optical properties in the projector-augmented wave methodology, Phys Rev B, 73 (2006) 045112.

[60] Y. Duan, P. Ohodnicki, B. Chorpening, H. Abernathy, G. Hackett, Theoretical Investigation of the Electronic Structural, Optical and Thermodynamic Properties of $La_xSr_{1-x}TiO_3$ (x=0, 0.125, 0.25), ECS Transactions, 78 (2017) 2865-2876.

[61] Y. Duan, P. Ohodnicki, B. Chorpening, G. Hackett, Electronic structural, optical and phonon lattice dynamical properties of pure- and La-doped $SrTiO_3$: an *ab initio* thermodynamics study, J Solid State Chem, submitted (2017).

[62] D.B. Tanner, Optical Effects in Solids, Department of Physics, University of Florida, 2016.

[63] M. Fox, Optical Properties of Solids, 1st ed., Oxford University Press, Oxford, 2001.

[64] D. Wiedemann, S. Indris, M. Meven, B. Pedersen, H. Boysen, R. Uecker, P. Heitjans, M. Lerch, Single-crystal neutron diffraction on gamma-$LiAlO_2$: structure determination and estimation of lithium diffusion pathway, Z Krist-Cryst Mater, 231 (2016) 189-193.

[65] B. Schulz, H. Wedemeyer, Preparation, Characterization and Thermal-Diffusivity of Gamma-$LiAlO_2$, J Nucl Mater, 139 (1986) 35-41.

[66] G.W. Hollenberg, D.E. Baker, Thermal properties of lithium ceramics for fusion applications, Annual Meeting of the American Ceramic Society, Cincinnati, OH, USA, 1982, pp. HEDL-SA-2674-FP.

3 Defect Chemistry of γ-$LiAlO_2$, Li_2ZrO_3, and Li_2TiO_3

3.1 Introduction

Ceramics such as γ-$LiAlO_2$, Li_2TiO_3, and Li_2ZrO_3 are considered candidates for their suitability as blanket materials in tritium-producing burnable absorber rods (TPBARs) [1-3]. After reacting with neutrons, lithium is readily converted to tritium (T, which is a ^3H isotope) in the lithium ceramic breeder blanket [4], and the bred tritium is further recovered from the blanket as HT and HTO with the addition of hydrogen to the purge gas. The defects and structural disorder may enhance the diffusion of Li and tritium within TPBAR materials. Due to lack of fundamental data such as hydrogen isotope solubility and diffusivity, currently, a detail understanding of the tritium transport in ceramic pellets and across barrier/cladding system is still not available [5-11].

In this study, we focus on DFT modeling of the trends in defect stability among the three material systems for the TPBAR applications. While the obtained defect energetic database can be further incorporated into *ab initio* based thermodynamic modeling to predict concentration of the defect species under equilibrium conditions [12-14], the defect concentration in the TPBARs blankets may be shifted from the equilibrium conditions due to the irradiation effects. Nonetheless, it has also been suggested that correlations exist between the annihilation of irradiation defects and the tritium release behavior of solid tritium breeding materials irradiated with neutrons [15-17], indicating not only tritium diffusion but also the interactions between tritium and irradiation defects could play important roles for the TPBAR applications. As a first step, we perform a comprehensive investigation of the thermodynamic defect stabilities among the three TPBAR materials γ-$LiAlO_2$, Li_2TiO_3, and Li_2ZrO_3 under various conditions, to serve as a theoretical foundation to cross validate with experimental characterizations as well as for providing guidance to model quantitatively the tritium transport and release in TPBAR materials. Such first principles based computational results can be combined with phase diagrams analysis for phase stability of the TPBAR materials.

3.2 Theoretical method

Spin polarized DFT calculations were performed with the Vienna *Ab-initio* Simulation Package (VASP)[18] using the Perdew–Burke–Ernzerhof (PBE) exchange-correlation functional,[19, 20] the Projector Augmented Wave (PAW) method,[21] and the plane wave basis sets with a cutoff energy of 550 eV. 2×2×2 128-atom, 2×1×2 96-atom, and 2×1×1 96-atom perfect bulk supercells are created for γ-$LiAlO_2$, Li_2ZrO_3, and Li_2TiO_3, respectively, from the optimized unit cells relaxed through DFT. The atomic positions of the defect containing supercells are then internally relaxed with fixed lattice constants and cell angles of the fully relaxed perfect bulk supercells.

The atomic positions in the defect supercells were relaxed at constant volume until the individual forces on each atom were <0.01 eV/Å. On the basis of the convergence tests of defect energies with the supercell size, the 2×2×2 $LiAlO_2$, 2×1×2 Li_2ZrO_3, and 2×1×1 Li_2TiO_3 supercells with 2×2×2 Monkhorst−Pack kpoint grid were used for defect calculations.

The calculated band gaps of γ-$LiAlO_2$, Li_2ZrO_3, and Li_2TiO_3 are 5.1 eV, 3.9 eV, and 3.1 eV respectively, which may potentially be underestimated due to inherent self-interaction error within the level of the DFT method using the Generalized-Gradient-Approximation (GGA) PBE functional. In this work, we focus on trends in defect stability among the three material systems for the TPBAR applications at the PBE level. These trends at the PBE level in defect stability among the three material systems for the TPBAR applications are expected to be sustained when using hybrid functionals to improve description of the band gaps [22].

Perfect (non-defective) bulk and point defect formation energy analysis was performed using the PyCDT module [23] based on the open-source Python Materials Genomics (pymatgen) software and the Materials Project database[24] for γ-$LiAlO_2$, Li_2ZrO_3, and Li_2TiO_3. The thermodynamic formalism proposed by Zhang and Northrup[25] was employed to calculate the formation energy of a point defect of type X with charge q, $\Delta E_{form}(Xq)$:

$$\Delta E_{form}(X^q) = E^T_{defec}(X^q) - E^T_{perf}[bulk] + \Sigma\, n_i\mu_i + q\mu_i + E_{corr} \quad (1)$$

where $E^T_{defec}(X^q)$ is the total energy of defect supercell, $E^T_{perf}[bulk]$ is the total energy of bulk supercell, μ_i is the chemical potential contribution due to the removal or addition of the atom, n_i

is the number of atoms removed or added in the supercell, μ_e is the Fermi level (chemical potential of the electron), and E_{corr} is the correction term. The implementation of the PyCDT module for the first principles based defect stability analysis has also been applied to the Cr_2O_3 material system in a recent study by Medasani *et al.* [26]. Table 3.1 summarizes the calculate charge defect species in the three γ-$LiAlO_2$, Li_2ZrO_3, and Li_2TiO_3 phases. Figure 8 shows their structures.

To correct for the long-range Coulomb interactions of charged defects between finite size periodic supercells, an extended Kumagai scheme[27] for the electrostatic correction method developed by Freysoldt *et al.*[28], which takes into account the anisotropy of the γ-$LiAlO_2$, Li_2ZrO_3, and Li_2TiO_3 phases, was applied to calculate E_{corr}.

Defect stability under various external environments was further accounted for by the setting of chemical potentials of the metal cations, oxygen anions, and tritium in metal oxides, and can be calculated using eq. 1. The elementary chemical potentials are selected from the computed entries in the Materials Project database based on the specified lower order phases formed by the constituent elements, as described in more detail at the beginning of Section 3.3. In most of the defect chemistry analysis results described below, hydrogen was used instead of tritium. It is noted that in this work only the 0 K DFT-computed phase stability is used for the analysis of defect stability among the γ-$LiAlO_2$, Li_2ZrO_3, and Li_2TiO_3 phases. The effects of pO_2, pH_2, and temperature are neglected in the present work but can be further incorporated through *ab initio* thermodynamic analysis by varying chemical potentials of the elements as a function of pO_2, pH_2, and temperature [12, 13].

3.3 Results and Discussion

Since oxygen activity is difficult to be measured as a unique quantity for the material system due to local chemical variations that can result in different gas phase composition/activity, two contrast scenarios are selected to demonstrate the quantitative changes in defect stability between the two corresponding chemical potential conditions: the oxygen-rich condition and the metal hydride rich condition. The latter condition is considered based on the experimental observation that metal hydride could be formed preferentially along the grain boundaries of the blanket materials[29] or regions that are closer to the metal getter materials.

Figure 9 shows the calculated defect formation energies of the charged defect species as a function of the Fermi level for γ-$LiAlO_2$, Li_2ZrO_3, and Li_2TiO_3 phases under the Li_2O_2–O_2–LiOH (oxygen-rich) condition. In the plots of Figure 9, the valence band maximum (VBM) of the perfect bulk is chosen as the reference energy and the vertical dashed dash lines in the plots indicate the conduction band minimum (CBM) as well as the band gaps. The formation energies of the defect species at different charge states listed in Table 3.1 are labeled in the right-hand-side legend of Figure 9. The slopes of the lines reflect on the charge state of the defect species and are also partially labeled in the first plot shown. Since the defect calculations are based on the same DFT-PBE functional, the calculated defect formation energies and the transition energy levels of the Ti vacancy and O vacancy in Li_2TiO_3 are consistent with those reported by Murphy *et al.*[12], whereas the Li vacancy formation energy is shifted down by approximately 0.5 eV due to use of different Li chemical potential references (Li_2O_2 in Figure 9 vs. Li_2O in Ref. [12]). Overall, the calculated Li_2TiO_3 defect stability results shown in Figure 9(c) are in good agreement with those reported in the previous DFT-PBE studies [12, 13], which indicates the charged defect analysis based on the PyCDT module [23] can be systematically utilized as a robust DFT defect modeling platform for extracting defect stability trends among different materials and phases.

For a given material system, one of the defect species that exhibit a prominent change in defect stability between the two selected chemical conditions is the H_O substitutional defect (another defect species is the metal vacancies which exhibit an opposite change vs. H_O in the stability between the two chemical conditions), as shown in Figure 10 vs. Figure 9. It can be seen in Figure 9 that formation of the H_O substitutional defects is highly energetically unfavorable under the Li_2O_2–O_2–LiOH (oxygen-rich) condition at T= 0 K, due to the large defect formation energies (+4~9 eV). The H_O substitutional defect can become greatly stabilized under or metal hydride-rich condition, as shown in Figure 10 where the selected chemical potential Li_3Al_2-Li_5AlO_4-LiH, Zr_3O–ZrO_2–ZrH_2, and $LiTi_2O_4$–$LiTiO_2$–TiH_2 conditions for the γ-$LiAlO_2$, Li_2ZrO_3, and Li_2TiO_3 systems are generated by the Python Materials Genomics (pymatgen) software and the Materials Project database[24], or in oxygen-poor condition at high temperatures[13]. The results revealed in Figure 10 indicate a significant stabilization of the H_O substitutional defect relative to those in the oxygen rich condition. It was also pointed out by Murphy [13] that the hydride ion occupying a doubly positively charged oxygen vacancy (*i.e.*, H_O^{1+}) is the stable species in Li_2TiO_3 under oxygen-poor conditions at high temperature (T=1000K). By comparing the H_O formation energy trends in both the oxygen-rich and metal-hydride rich conditions among the three material systems, the stability order found is as follows: γ-$LiAlO_2$ > Li_2ZrO_3 > Li_2TiO_3.

3.4 Summary

In this work, a systematic defect stability analysis as a function of electron chemical potential under two selected chemical potential conditions (oxygen-rich and metal hydride rich conditions) is performed for the γ-$LiAlO_2$, Li_2ZrO_3, and Li_2TiO_3 materials for the TPBAR applications, based on the DFT-PBE modeling and the PyCDT module [23] as implemented in the framework of Python Materials Genomics and the Materials Project database[24]. The calculated defect stability results of Li_2TiO_3 are in good agreement with the previous results by Murphy et al. [12, 13], whereas the thermodynamic analysis using the PyCDT module of pymatgen allows to consistently extract the defect stability information for comparison among the selected materials systems. Our results demonstrate that the H_O substitutional defect can become more stable under oxygen-poor or hydrogen-rich conditions, which is consistent with the experimental observations that tritium trapping/detrapping at oxygen vacancies could potentially control the tritium release and transport in the TPBAR materials [15-17]. The extracted H_O formation energy trend under the metal hydride rich condition (also the oxygen rich condition) is as follows: γ-$LiAlO_2$ > Li_2ZrO_3 > Li_2TiO_3. Overall, our results provide a theoretical foundation to further cross validate with experimental defect configurations/characterizations in the TPBAR materials as well as in a wide range of chemical potential conditions.

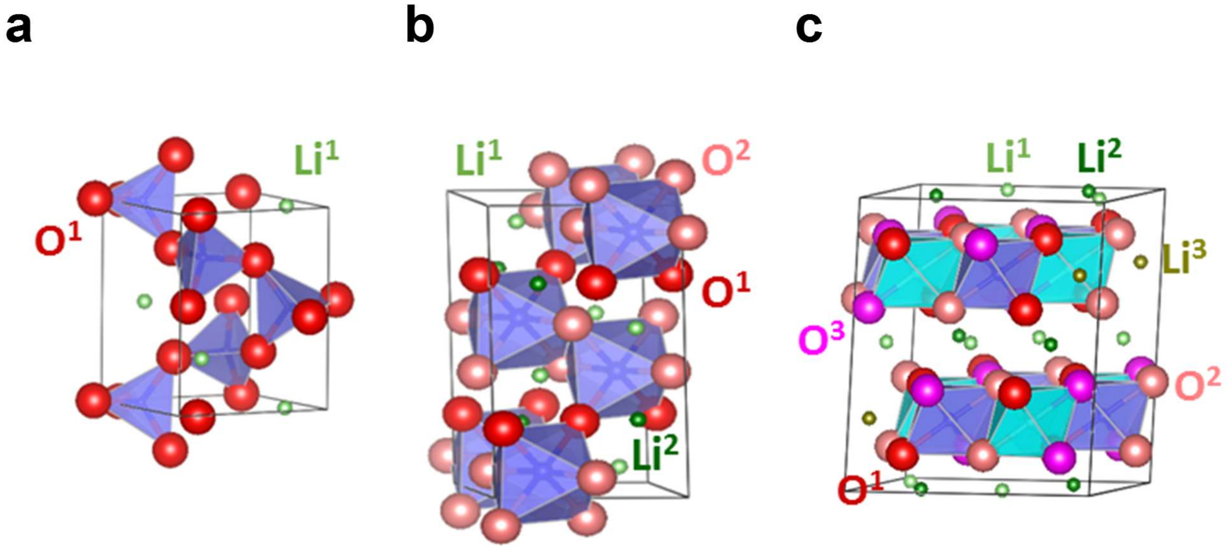

Figure 8 The crystal structures of (a) γ-$LiAlO_2$, (b) Li_2ZrO_3, and (c) Li_2TiO_3 phases investigated in this work. Symmetry distinct Li and O sites labeled with different superscripts are presented in green (light, dark, and olive) and red (light, dark, and magenta) color, respectively. Blue atoms in the center of polyhedra are the metal cations of Al, Zr, and Ti (with light and dark blue for different Ti site).

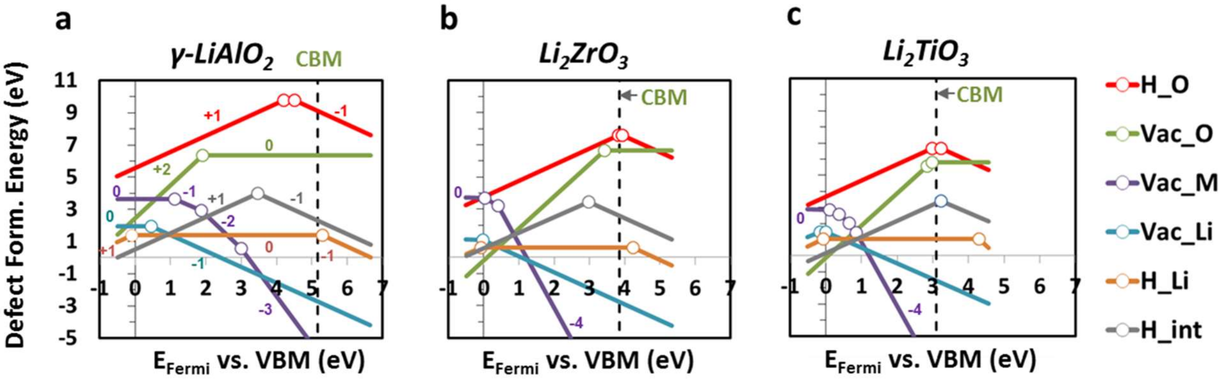

Figure 9 The calculated defect formation energies of the charged defect species of (a) γ-$LiAlO_2$, (b) Li_2ZrO_3, and (c) Li_2TiO_3 phases as a function of Fermi level (E_{Fermi}) under the Li_2O_2–O_2–LiOH (oxygen-rich) condition. For the Fermi level, the valence band maximum (VBM) of the perfect bulk is chosen as the reference energy and the vertical dashed line in the plots indicates the conduction band minimum (CBM) as well as the band gap of the material. Due to the large scale of the y-axis that spans a 16 eV range, energy differences for a given defect species at symmetry distinct sites are within the line width and therefore not presented in the plots.

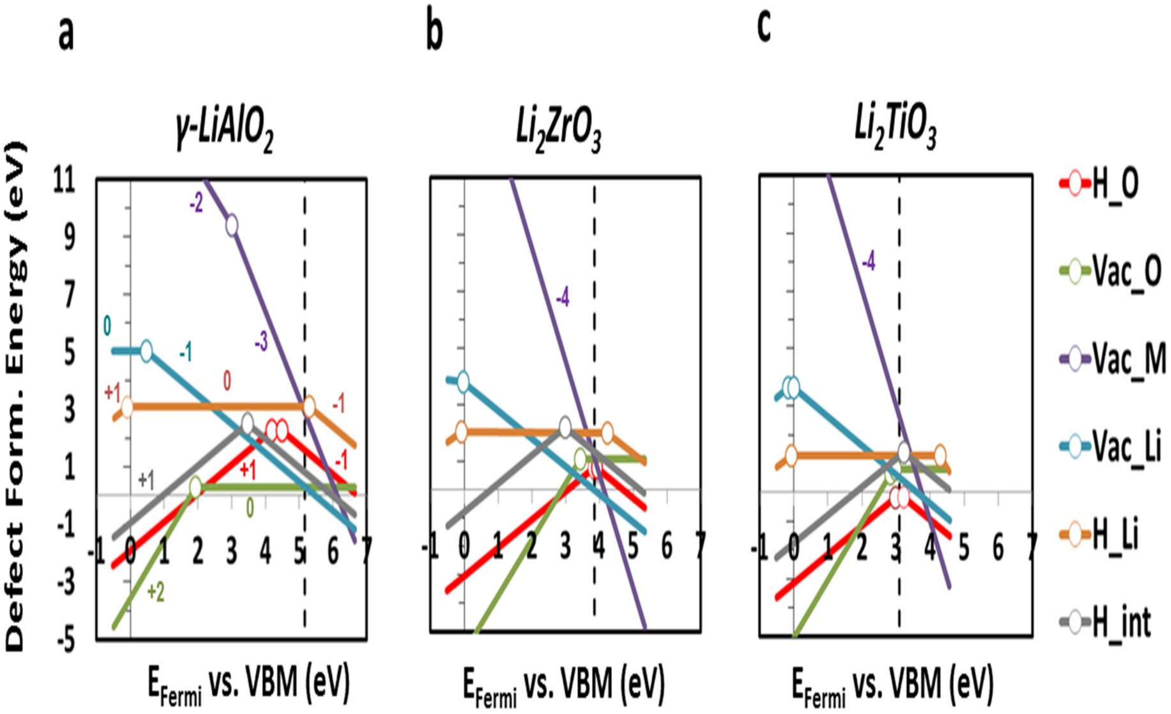

Figure 10 The calculated defect formation energies of the defect species as a function of Fermi level (E_{Fermi}) under the (a) Li_3Al_2-Li_5AlO_4-LiH, (b) Zr_3O–ZrO_2–ZrH_2, (c) $LiTi_2O_4$–$LiTiO_2$–TiH_2 conditions for γ-$LiAlO_2$, Li_2ZrO_3, and Li_2TiO_3 respectively. For the Fermi level, the valence band maximum (VBM) of the perfect bulk is chosen as the reference energy and the vertical dashed lines in the plots indicate the conduction band minimum (CBM) as well as the band gap of the material. Due to the large scale of the y-axis that spans a 16 eV range, energy differences for a given defect species at symmetry distinct sites are within the line width and therefore not presented in the plots.

Table 3.1 Charge states of the defect species calculated in this work. The defect species include Li vacancy (V_{Li}), metal vacancy (V_M; M= Al, Zr, and Ti), oxygen vacancy (V_O), ^3H substitution on a Li site ($^3H_{Li}$), ^3H substitution on an oxygen site (^3H_O), and ^3H interstitial in the crystal ($^3H_{int}$). The superscript "3" in front of H is to denote it as a hydrogen-3 isotope. The number of symmetry distinct sublattice sites in the structure is presented in the parenthesis in the columns of "Sites".

Defect type	Label	γ-$LiAlO_2$ (2×2×2, 128-atom-cell)		Li_2ZrO_3 (2×1×2, 96-atom-cell)		Li_2TiO_3 (2×1×1, 96-atom-cell)	
		Sites	Charge	Sites	Charge	Sites	Charge
Vacancy	V_{Li}	Li(1)	0, -1	Li(2)	0, -1	Li(3)	0, -1
	V_M	Al(1)	0, -1, -2, -3	Zr(1)	0, -1, -2, -3, -4	Ti(2)	0, -1, -2, -3, -4
	V_O	O(1)	+2, +1, 0	O(2)	+2, +1, 0	O(3)	+2, +1, 0
^3H Substitution	$^3H_{Li}$	Li(1)	+1, 0, -1	Li(2)	+1, 0, -1	Li(3)	+1, 0, -1
	^3H_O	O(1)	+1, 0, -1	O(2)	+1,0, -1	O(2)	+1,0, -1
^3H Interstitial	$^3H_{int}$	Int(n^*)	+1, 0, -1	Int(n^*)	+1, 0, -1	Int(n^*)	+1, 0, -1
Total defect configurations		$15+3\times n^*$		$27+3\times n^*$		$40+3\times n^*$	

n^*: number of configurations from manual insertion of ^3H *($n^* \geq 3$)*

3.5 References

1. Johnson, C.E., *Tritium behavior in lithium ceramics.* Journal of Nuclear Materials, 1999. **270**(1): p. 212-220.
2. Roux, N., et al., *Ceramic breeder material development.* Fusion Engineering and Design, 1998. **41**(1): p. 31-38.
3. Johnson, C.E., K. Noda, and N. Roux, *Ceramic breeder materials: Status and needs.* Journal of Nuclear Materials, 1998. **258**(Part 1): p. 140-148.
4. Senor, D.J., *Recommendations for Tritium Science and Technology Research and Development in Support of the Tritium Readiness Campaign, TTP-7-084*. 2014, PNNL.
5. Okuno, K. and H. Kudo, *Diffusion-Controlled Tritium Release from Neutron-Irradiated Gamma-$LiAlO_2$.* Journal of Nuclear Materials, 1986. **138**(2-3): p. 210-214.
6. Okuno, K. and H. Kudo, *Tritium diffusivity in lithium-based ceramic breeders irradiated with neutrons.* Fusion Engineering and Design, 1989. **8**: p. 355-358.
7. Ono, F., S. Tanaka, and M. Yamawaki, *Tritium sorption by cement and subsequent release.* Fusion Engineering and Design, 1995. **28**: p. 378-385.
8. Badawi, A., A.R. Raffray, and M.A. Abdou, *Analysis of Tritium Release from LiAlO2 in the Tequila Experiment, Using the Mistral Code.* Fusion Engineering and Design, 1991. **17**: p. 73-78.
9. Carrera, L.M., et al., *Tritium recovery from nanostructured $LiAlO_2$.* Journal of Nuclear Materials, 2001. **299**(3): p. 242-249.
10. Nishikawa, M., et al., *Release behavior of bred tritium from $LiAlO_2$.* Journal of Nuclear Materials, 2004. **335**(1): p. 70-76.
11. Oyaidzu, M., et al., *Correlation between annihilation of radiation defects and tritium release in neutron-irradiated $LiAlO_2$.* Fusion Science and Technology, 2005. **48**(1): p. 638-641.
12. Murphy, S.T. and N.D.M. Hine, *Point Defects and Non-stoichiometry in Li_2TiO_3.* Chemistry of Materials, 2014. **26**(4): p. 1629-1638.
13. Murphy, S.T., *Tritium Solubility in Li_2TiO_3 from First-Principles Simulations.* The Journal of Physical Chemistry C, 2014. **118**(51): p. 29525-29532.
14. Nowotny, J., et al., *Towards sustainable energy. Generation of hydrogen fuel using nuclear energy.* International Journal of Hydrogen Energy, 2016. **41**(30): p. 12812-12825.
15. Moriyama, H., S. Tanaka, and K. Noda, *Irradiation effects in ceramic breeder materials.* Journal of Nuclear Materials, 1998. **258**(Part 1): p. 587-594.
16. Okuno, K. and H. Kudo, *Chemical states of tritium and interaction with radiation damages in Li_2O crystals.* Journal of Nuclear Materials, 1986. **138**(1): p. 31-35.
17. Kobayashi, M., Y. Oya, and K. Okuno, *Migration of hydrogen isotopes in lithium metatitanate.* Journal of Nuclear Materials, 2013. **439**(1): p. 159-167.
18. Kresse, G. and J. Furthmuller, *Efficient iterative schemes for ab initio total-energy calculations using a plane-wave basis set.* Physical Review B, 1996. **54**(16): p. 11169-11186.
19. Perdew, J.P., K. Burke, and M. Ernzerhof, *Generalized gradient approximation made simple.* Physical Review Letters, 1996. **77**(18): p. 3865-3868.
20. Blochl, P.E., *Projector Augmented-Wave Method.* Physical Review B, 1994. **50**(24): p. 17953-17979.
21. Kresse, G. and D. Joubert, *From ultrasoft pseudopotentials to the projector augmented-wave method.* Physical Review B, 1999. **59**(3): p. 1758-1775.
22. Ramprasad, R., et al., *New Perspective on Formation Energies and Energy Levels of Point Defects in Nonmetals.* Physical Review Letters, 2012. **108**(6): p. 066404.
23. Broberg, D., et al., *PyCDT: A Python toolkit for modeling point defects in semiconductors and insulators.* ArXiv e-prints, 2016. **1611**: p. arXiv:1611.07481.

24. Ong, S.P., et al., *Python Materials Genomics (pymatgen): A robust, open-source python library for materials analysis.* Computational Materials Science, 2013. **68**(Supplement C): p. 314-319.
25. Zhang, S.B. and J.E. Northrup, *Chemical potential dependence of defect formation energies in GaAs: Application to Ga self-diffusion.* Physical Review Letters, 1991. **67**(17): p. 2339-2342.
26. Medasani, B., et al., *Vacancies and Vacancy-Mediated Self Diffusion in* Cr_2O_3*: A First-Principles Study.* The Journal of Physical Chemistry C, 2017. **121**(3): p. 1817-1831.
27. Kumagai, Y. and F. Oba, *Electrostatics-based finite-size corrections for first-principles point defect calculations.* Physical Review B, 2014. **89**(19): p. 195205.
28. Freysoldt, C., J. Neugebauer, and C.G. Van de Walle, *Fully Ab Initio Finite-Size Corrections for Charged-Defect Supercell Calculations.* Physical Review Letters, 2009. **102**(1): p. 016402.
29. Jiang, W., et al., *Nanostructural evolution and behavior of H and Li in ion-implanted* γ-$LiAlO_2$. Journal of Nuclear Materials, 2017. **494**(Supplement C): p. 411-421.

4 Tritium Diffusion Pathways in γ-$LiAlO_2$ and Li_2ZrO_3

4.1 Background

In sections 2 and 3, we discussed the bulk properties and the defect chemistry of the ceramic materials γ-$LiAlO_2$ and Li_2ZrO_3. Another important property which we want to discuss next is related to the diffusion pathways of tritium (T) species. The understanding of the fundamental properties, in particular related to defect chemistry, is of vital importance to identify the corresponding diffusion mechanism. A recent molecular dynamics simulation on defect accumulation and ion transport in $LiAlO_2$ revealed that at 573 K a rapid lattice disorder (0.1~0.2 displacement per atom) takes place at a sufficiently high simulated neutron irradiation dose leading to full amorphization of the lattice and an increase in Li diffusivity by 30 times [1]. The Li diffusion in this material has been studied using ab initio methods [2]. There are also experimental results available for Li diffusion using different techniques [3, 4, 5]. Shah et al [6, 7] performed ab initio calculations to understand the dependence on temperature of the T diffusion mechanism in Li_2O, and predicted that an upper limit of T diffusion barrier is 0.45 eV corresponding to interstitial T diffusion. In addition to that, it is unclear whether T exists as an interstitial or as a substitutional defect. Despite the availability of Li diffusivity data, so far T diffusion mechanism in the ceramic pellets is not well understood. Here we present the results of first-principles density functional theory (DFT) calculations of interstitial and substitutional T defects, hydroxide (O-T) vacancy defect, the interaction of T with O-vacancies in ceramic materials γ- $LiAlO_2$ and Li_2ZrO_3, and provide an understanding of how such defects hamper the diffusivity and solubility of T. By considering several different diffusion pathways, we examine the possible activation barrier heights of T as well as of O-T species as single entities when migrating as an interstitial defect or as a substitutional defect. To follow the experimental approach of obtaining results at different T concentrations, we calculate the T diffusion behavior at various concentrations in the crystal. Our results show that the smallest activation barrier height is 0.63 eV and corresponds to the substitutional T diffusion. The smallest O-T diffusion barrier height is found to be 3.5 eV which is several times higher than that of the T alone diffusion. This finding suggests that O-T diffusion as a single entity is less probable.

4.2 Computational Method

We use first principles DFT approach with Perdew-Burke-Ernzerhof (PBE) functional [8, 9] based on the generalized gradient approximation (GGA) as implemented in the Vienna ab initio Simulation Package (VASP) [10, 11]. The core electrons are represented by projected-augmented wave (PAW) method. The plane wave cut-off energy of 400 eV is used, and the total energy convergence is obtained within an accuracy of 0.01 eV. For higher cut-off energies, lattice parameters are changed by less than 0.02 Å, suggesting that an acceptable energy convergence criterion has been met. The reciprocal space integration is performed with the Monkhorst-Pack grid of 7x7x7 for the unit cell structure, and the energy convergence of 10^{-6} eV was achieved. The structures are fully relaxed until a threshold of 0.01 eV/Å was achieved prior to the calculations of defect and diffusion properties. Diffusion calculations were performed using a 2x2x2 supercell (corresponding to $Li_{32}Al_{32}O_{64}$ system) for which a 2x2x2 Monkhorst-Pack grid was used to sample the Brillouin zone. The climbing-image nudged elastic band approach (cNEB) was used to map the diffusion pathways among different local minima.

4.3 Diffusivity and Solubility in L_iAlO_2

The six vertices of XO_4 (X = Li, Al) tetrahedra form a slightly distorted three dimensional (3D) hexagonal geometry around the center of the unit cell. The distorted 3D hexagonal geometry consists of two opposite facets of nearly rectangular shape each lying nearly in the (110) plane with different metal tetrahedra sharing one edge diagonally as shown in the Figure 11.

Neutron irradiation of the γ-LiAlO2 can induce different types of defects and vacancies. An important question is to understand how T diffuses in the defected crystal. When a Li is substituted by T as a substitutional defect (T_s), it makes a hydroxide type bond with the nearby O. The Ts leaves Li vacancy (V_{Li}) position and moves toward O by 0.91 Å. This is the most stable position of the T_s. The calculated distance of OT bond in this case is 0.98 Å and is directed toward the V_{Li}. We find that rotation of OT bond in (101) plane by 25° to position the entire OT group for migration as discussed in section 4.3.4 increases repulsive interaction 0.2 eV. Similarly, an interstitial T (T_i) and O bond has no rotational symmetry around O, and therefore, T_i cannot freely move around O unlike one find in case of Li_2O system [3]. Here we have three species of atoms that create a less symmetric environment in the crystal.

4.3.1 Substitutional T (T_s) migration

The analysis of the migration properties of T at low concentration levels can provide a valuable insight, and can be directly correlated with future experimental observations on T diffusion properties. This has been done by considering a T_s in a 2x2x2 supercell (3.12 % concentration) containing a total of 128 atoms. The T_s associated with a particular V_{Li} in one of the LiO_4 tetrahedra in the distorted hexagonal structure, as shown in the Figure 11, can migrate to other empty LiO_4 tetrahedron either in the same structure or in the one lying adjacent to it. When T_s moves to V_{Li} in the first nearest neighbor (1st NN, see Figure 12 for the definition of NN) position, the most probable pathway is to migrate along the facet of distorted hexagon. In this case, we calculate an activation energy barrier (E_{act}) to be 0.63 eV as shown in the Figure 12 **a**. The energy barrier of 0.58 eV for T_s migration in Li_2O [6, 7], and 0.65 eV for the Li migration in γ -$LiAlO_2$ have been reported [2].

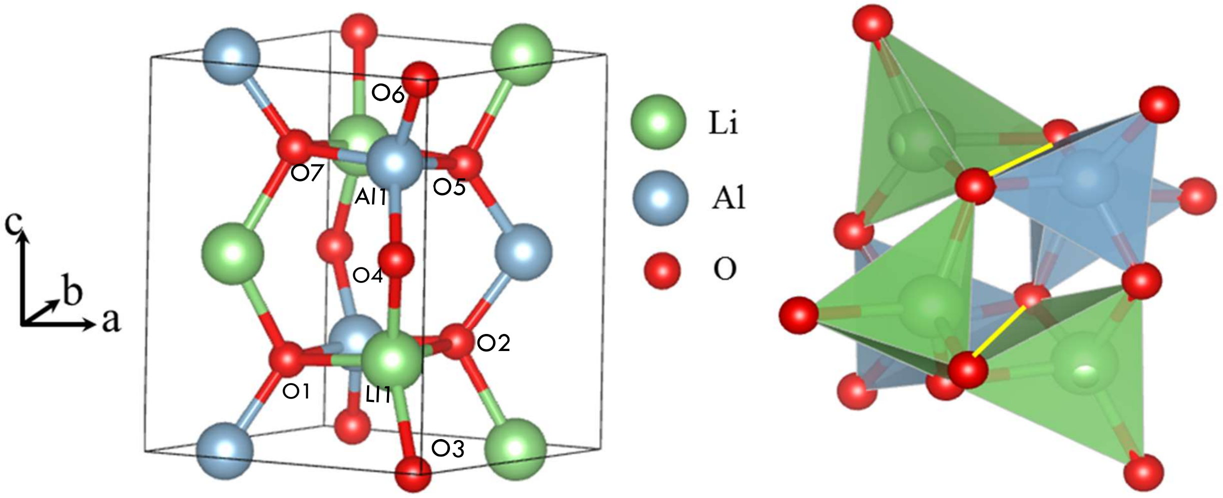

Figure 11 Unit cell of **γ** –$LiAlO_2$ (**a**), the shared edges of XO_4 (X = Li, Al) tetrahedra (green color-Li tetrahedra, and light blue color-Al tetrahedra) are highlighted with yellow color and lie opposite facet of the 3D hexagonal structure (**b**).

In the Figure 12 **b** and **c**, we also show that E_{act} when T_s migrates to V_{Li} position located at 2nd and 3rd NN neighbors whose optimized distances are 4.18 Å and 4.94 Å, respectively. In a distorted hexagon, as shown in the Figure 11 **a**, 2nd NN lies in the diagonally opposite corners, whereas 3rd NN neighbor forms one of the vertices of the adjacent distorted hexagon. In each case, T migrates by making a bond with O, rotating about O, and finally breaking the bond. The E_{act} for migration to 2nd NN V_{Li} position is found to be 1.51 eV while for migration to the 3rd NN V_{Li} it is 0.86 eV. The peak in the barrier while migrating to 2nd NN V_{Li} position arises due to an inward pulling of OT bond toward the center of the distorted polygon that leads to a higher repulsive force. During the diffusion, the OT bond rotates by an angle of 48° in (101) plane around O, process that requires an energy of 0.85 eV. There is region of higher repulsion in between two distorted polygons through which T moves while migrating to 3rd NN V_{Li} position.

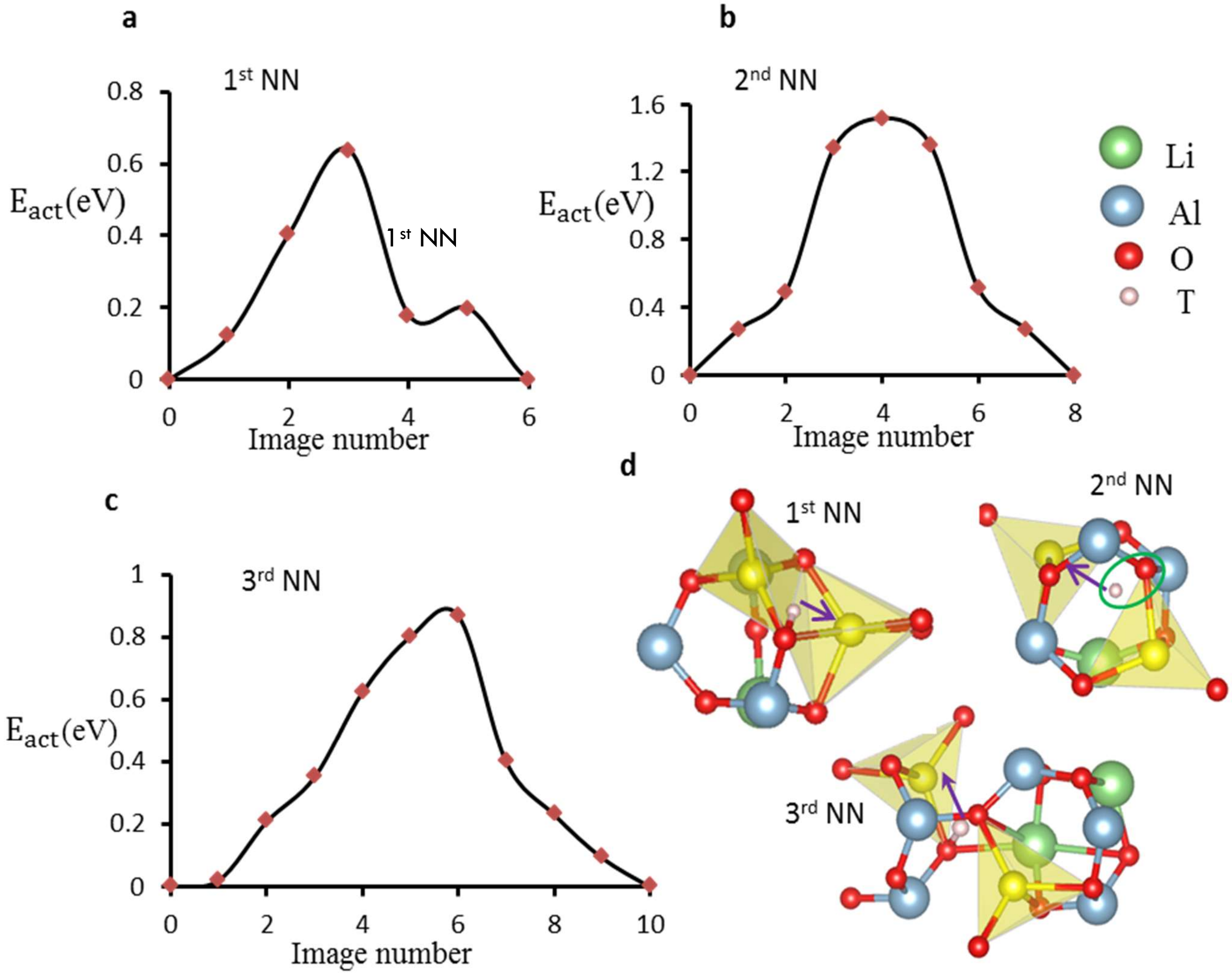

Figure 12 Activation energy barriers and transition pathways for T_s migration to the 1st (**a**), 2nd (**b**), and 3rd (**c**) NN $\mathbf{V_{Li}}$ position for which the distances are 3.12, 4.18 and 4.94 Å**,** respectively. In Figure (**d**) we present the transition states for the peak positions in (**a**), (**b**), and (**c**). The purple arrow indicates a transition direction. The green, blue, red and purple color spheres are for Li, Al, O and T respectively. In this Figure, we also show the tetrahedra around each Li vacancy.

The orientation of the OT group at the transition state is made possible by stretching O-Li bonds that leads to a peak in the migration profile energy as it passes by the empty space.

Our results for T diffusion are consistent with the results for Li diffusion between V_{Li} sites in γ –$LiAlO_2$ [11]. It is to be noted that center of the hexagon is a point of high symmetry where interaction between T and O is long range. The Table 4.1 summarizes the energy barriers for vacancy assisted diffusion.

We also calculate activation barriers when two T_s (6.25 % defect concentration) are at the 1st NN V_{Li} positions, and are diffusing to the V_{Li} positions each of which is a 3rd NN at distance of 4.94 A from each T_s (not shown here). The activation energy barrier is found to be 1.54 eV. This is higher by 0.68 eV than the single T_s migration barrier to 3rd NN.

Table 4.1 Activation energy for a substitutional T

Nearest Neighbor	1st NN	2nd NN	3rd NN
Distance (Å)	3.12	4.18	4.94
Activation Energy (eV)	0.63	1.51	0.86

4.3.2 Interstitial T (T_i) migration

In the interstitial migration with a Frenkel defect (with a T_i and a V_{Li}), Ti passes through the center of hexagon which is a region of high symmetry and the empty region as shown by the shaded plane in the Figure 13 **c.** As T_i passes through the center, first O moves inward as it forms a bond with Ti stretching O-Li bonds by around 1 Å, and then OT bond breaks as Ti moves further. This increases a repulsive interaction of

Ti with neighboring Li's giving rise to a peak barrier of 1 eV (peak A). As the Ti moves through the shaded region it passes the region of high symmetry that give rises to the peak B in the Figure 13 **a**.

To study the correlated motion of T, we calculate the energetic of the transition states for two T_i migrations to V_{Li} positions. The initial state in this case is higher by 0.85 eV than single T_i migration as can be seen from the energy difference of the initial images in the Figure 13 **a** and **b**. The activation barrier in this case is obtained to be 1.29 eV.

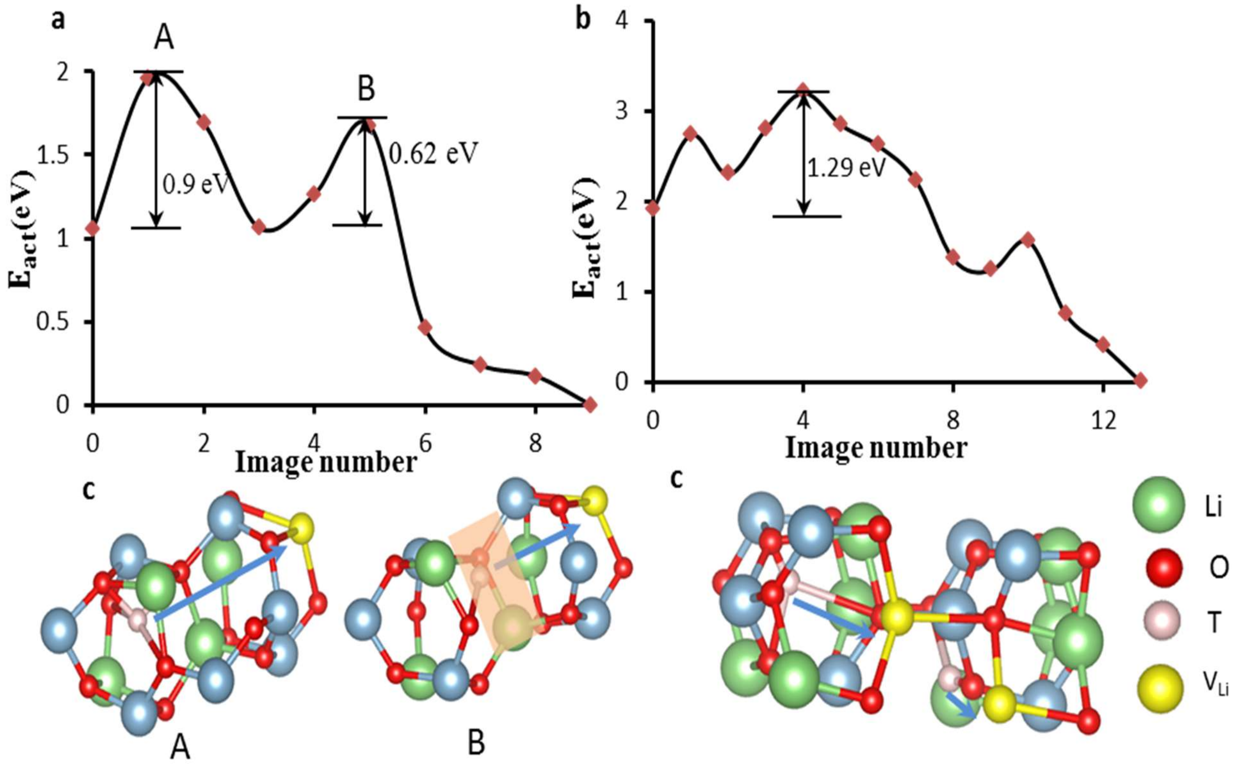

Figure 13 Interstitial migration of one T_i (a), and two T_i (b) to V_{Li}. The corresponding transition states for (**a**) is shown in (**c**) for peaks A and B (region between two hexagons is shown by the shaded orange plane), and the transition state for (**b**) is shown in (**d**) for the highest peak position. The color codes are as shown.

4.3.3 Li-T correlated migration

Next, we proceed to calculate migration pathways for correlated motion of Li and T_s. In the Figure 14 we present an activation energy barrier profile for a Li and a T_s swapping their positions when T is substituted in the 1st, 2nd and 3rd NN V_{Li} positions. First, a Li moves and a vacancy is created in each case. Then T_s migrates to V_{Li} position. To reduce repulsive interaction energy and force imbalance, T_s migrates by forming a OT bond, and the migrating Li can take pathways through the middle of the distorted hexagon while moving to such as V_{Li} which is 2nd NN. In case of 2nd NN, the barrier is significantly higher than 1st and 3rd NN position swapping due to a highly-curved migration pathway of T_s as it diffuses outside of hexagon while Li migrates diagonally through the middle region. The other possibility would be T_s taking a diagonal pathway while Li moves by a curved path. This mechanism would have an increased repulsive interaction as radius of sphere for minimum O-Li bond should not be less than 1.96 Å.

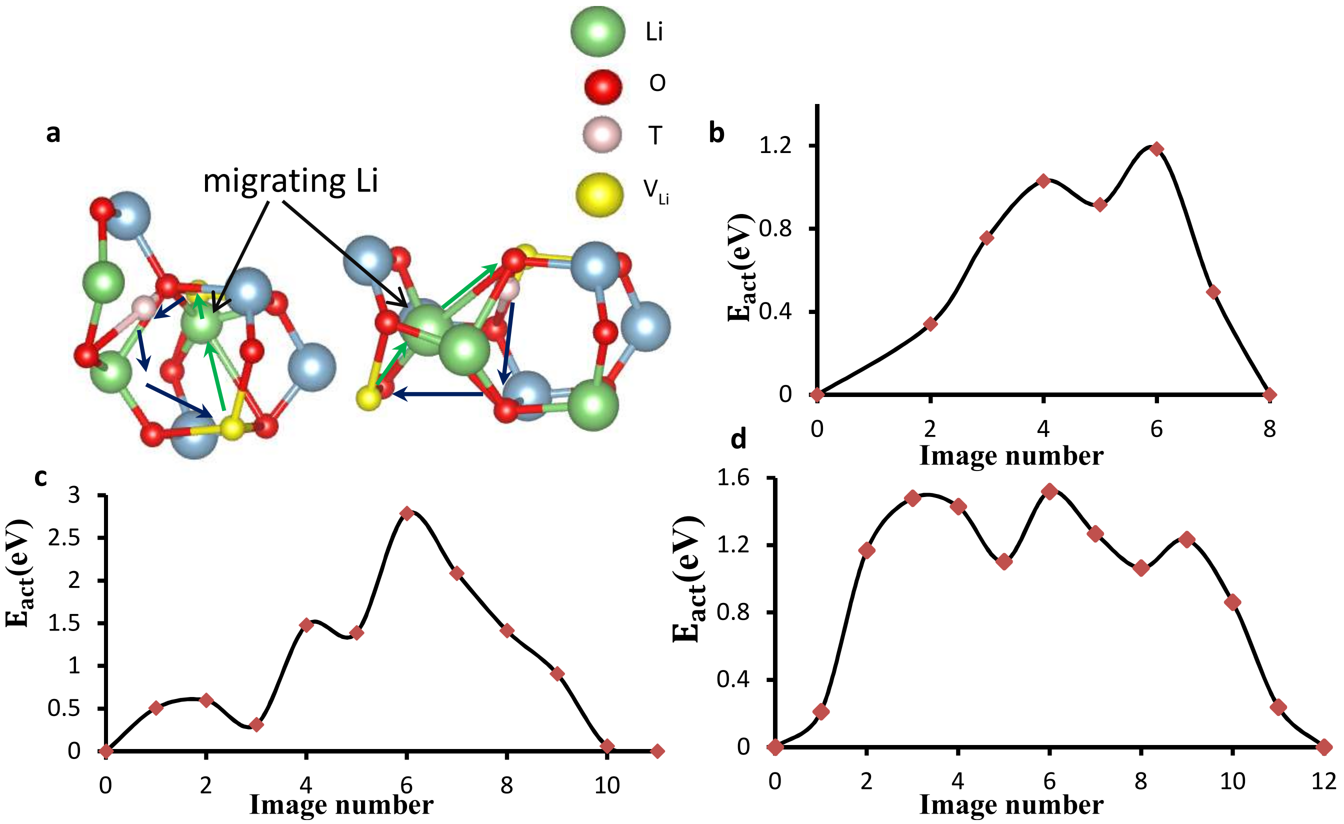

Figure 14 The schematic of migration energy pathways for Li and T swapping their positions at (**a**) 2nd NN, and 3rd NN vacancy positions. The activation energy barriers for (**b**) 1st, (**c**) 2nd and (**d**) 3rd NN migration by swapping positions are 1.18 eV, 2.78 eV and 1.51 eV, respectively. The arrows in (**a**) are pathways for Li (green) and for T (dark blue). The atom color codes are as shown.

4.3.4 OT migration

So far, we have discussed the defects and diffusion mechanisms for substitutional, interstitial, and Li-T correlated migrations. The other important type of vacancy creation in the radiation damaged crystal is bound O and Li vacancy (V_{OLi}). These vacancies can be occupied by migrating hydroxyls (OT) from neighbor sites depending up on the activation barriers. To study the OT diffusion mechanism and explore the pathways, we perform calculation for O and substituted T migrating as a bound entity to the 1st, 2nd and 3rd NN V_{OLi} positions. As shown in the Figure 15, the activation energy barrier is 2.17 eV for the OT migration to the V_{OLi} available at the 1st NN position, while it is 4.23 and 3.44 eV, respectively for the OT migration to the V_{OLi} available at 2nd and 3rd NN position. It is again to be noted that while migrating to the V_{OLi} at the 2nd NN position, barrier is higher than for the migration to the V_{OLi} at 1st and 3rd NN position. This is because OT passes through the highest symmetry region (moving around the center of hexagon) along with a rotation of the OT bond by approximately 25° in a-c plane. As OT migrates to V_{OLi} available at 3rd NN position, it passes through the empty region between the two hexagons where it experiences the highest repulsive interaction from the nearby ions which leads to a barrier of 3.44 eV as shown in the Figure 15 **c**.

4.3.5 Higher concentration of Li defect and T

The activation energy barrier for T diffusion can change with the increasing number of V_{Li} and T in the system. In experiment, neutron irradiation can create randomly distributed Li vacancies, and after recoil T can occupy either one of those vacancies or the interstitial site. In the thermodynamics equilibrium, the occupation probability of vacancies and interstitial sites by atoms is directly proportional to the Boltzmann factor, $e^{-\frac{E}{K_B T}}$, where K_B is a Boltzman constant and E is the energy barrier, times the number of available vacancies and other empty sites around the diffusing atoms. The occupation probability can be affected by the interaction energy of diffusing atoms with the surrounding environment as occupancy can decrease with increasing repulsive interaction and vice versa. The other important factor is that higher defect concentration can reduce symmetry of the system. In a system where symmetry is lowered, interaction can be significantly increased due to anisotropy in force, leading to a change in energy barrier for diffusion. It is computational intensive in DFT to calculate at higher concentration as it requires a large defective supercell size. Nevertheless, it is always possible to obtain some insight on the effect of increasing number of defects on the diffusion barriers and the pathways. As an example, we calculate the diffusion barrier by taking four Frenkel defects (V_{Li} + T_i). The calculated energy barrier is 3.41 eV. This energy barrier is higher by 2.51 eV for T_i diffusion in case of one Frenkel defect and 2.12 eV for T_i diffusion in case of two Frenkel defect.

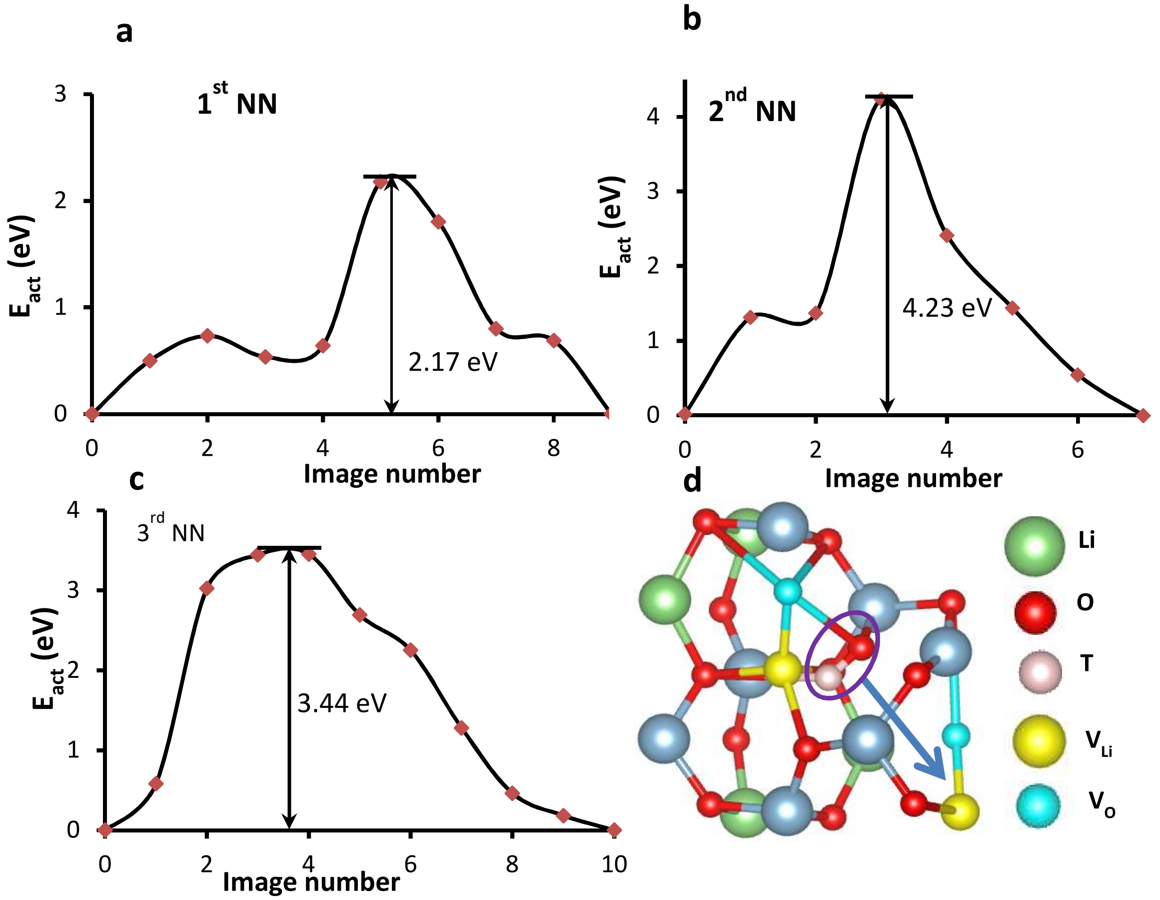

Figure 15 The OT diffusion to the bound Li and O vacancy (V_{OLi}) at (**a**) 1st NN, (**b**) 2nd NN, and (**c**) 3rd NN. The energy activation barrier in each case is 2.17 eV, 4.23 eV, and 3.44 eV. The Figure **d** shows a transition state of OT migrating to 3rd NN position. The color codes are as shown.

4.3.6 Diffusion Coefficient

Using the Einstein-Smoluchowski relation [12], it is possible theoretically to calculate the diffusivity and probability of jump per second for T diffusing to nearest empty site. The diffusion coefficient can be written as $D = \frac{a^2}{c\tau}$, where a and τ are average distance and time between two jumps, respectively, and c is 2 in 1D, 4 in 2D, and 6 in 3D. The quantity τ is proportional to the Boltzmann's factor that gives a probability of jump from one site to other. Therefore, diffusion coefficient can be written as $D \approx \frac{a^2}{6} R_o z e^{-\frac{(E_m + Q_V)}{k_B T}}$, where R_o is attempt frequency, and z is coordination number. The E_m is the migration barrier, and Q_V is the energy to form a vacancy. The probability of jump can be obtained from $\tau \approx \frac{1}{R_o z} e^{\frac{(E_m + Q_V)}{k_B T}}$. Assuming that we have crystal with a vacancy ($Q_V = 0$), and using the smallest energy barrier of 0.63 eV obtained for a substitutional T migrating to the 1st NN, we obtain about 1400 jumps/s at 300 K, whereas about 2 million jumps/s at 600 K.

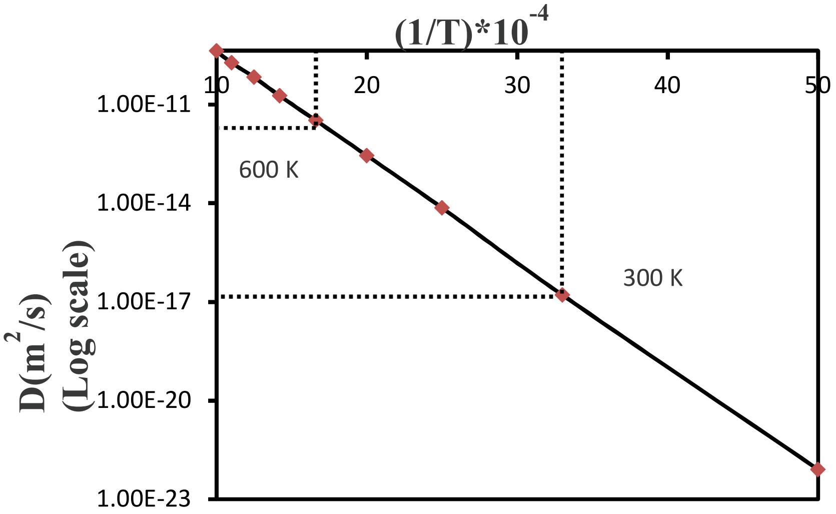

Figure 16 Diffusion coefficient in Log scale for LiAlO2

The calculated diffusion coefficient is shown in the Figure 16. From this, it is possible to obtain a qualitative description of the diffusivity of T in a low Li defect concentration limit.

4.4 Diffusivity and Solubility in Li_2ZrO_3

The crystal of Li_2ZrO_3 has monoclinic structure and has a symmetry of C2/c [13]. The symmetry is greatly lowered as compared to $LiAlO_2$ ($P4_12_12$). The details of the lattice parameters and structures are calculated by us previously, and can be found in the ref. [14]. In $LiAlO_2$ crystal, due to its high symmetry, there were several diffusion pathways possible as many of them are equivalent in term of energy barrier. However, in Li_2ZrO_3, due to its low-symmetry in nature, diffusing atom can have fewer number of isotropic diffusion pathways.

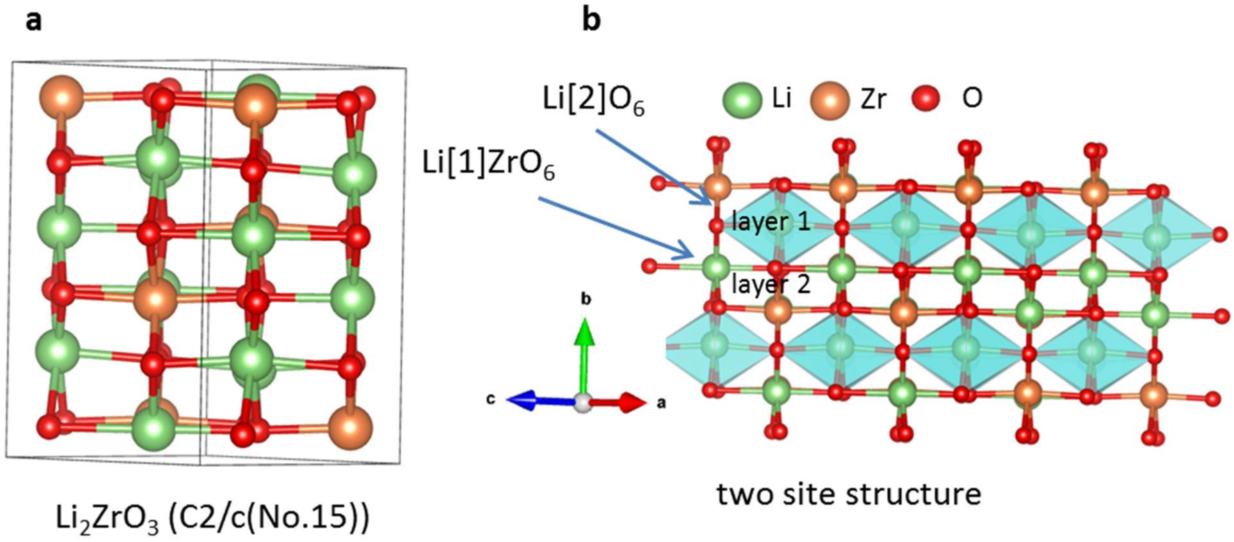

Figure 17 The monoclinic lattice (**a**) and two-layer model structure (**b**) of $LiZrO_3$. The two layers in (**b**) are formed by Li[1] in combination with O and Li[2] in combination with Zr and O. Li[1] and Li[2] represent the first and second type atoms of Li. Color codes are as shown on the top.

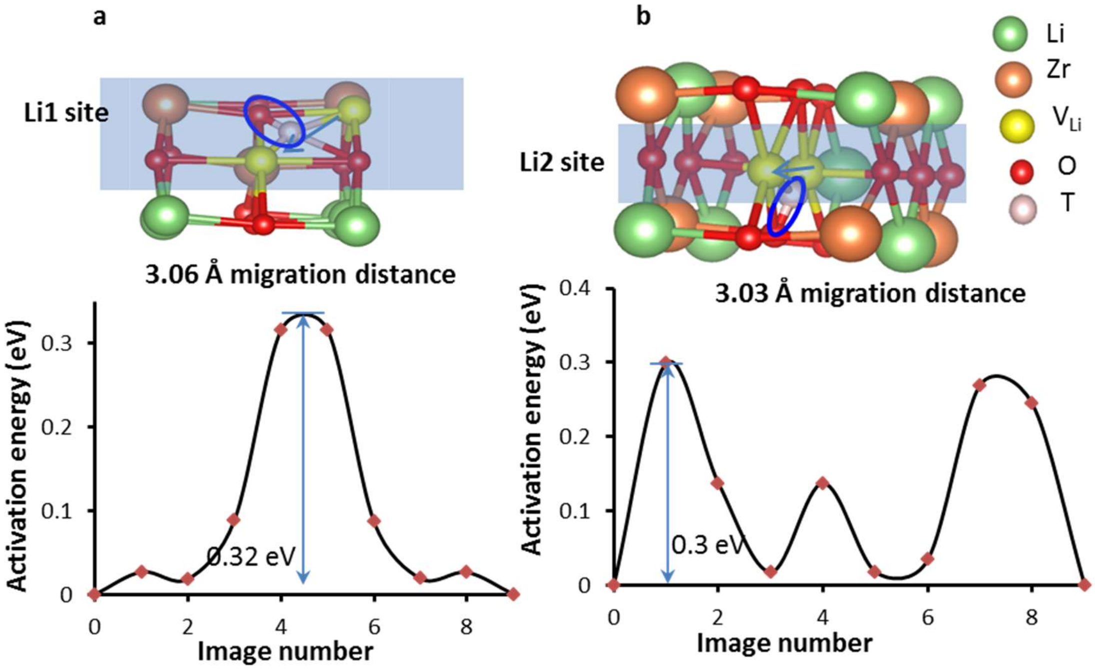

Figure 18 The vacancy assisted migration of the T in layer 1 and layer 2. The diffusion energy barrier for the migration within layer 1 is 0.32 eV (**a**) while within the layer 2 is 0.3 eV (**b**).

In the Figure 17 we present a lattice structure (**a**) and a model of two-layer structure (**b**) where first and second types of Li atom in combination with Zr and O form two alternating layers lying perpendicular to b axis. It is to be noted that in addition to the Li, there are two types of O based on the symmetry, O[1] bonded to Li[2] and O[2] bonded to Li[1]. The calculated bond lengths O[1]-Li[2] and O[2]-Li[1] are, respectively, 2 Å and 2.14 Å. Therefore, diffusing atom can see a different oxygen environment during migration.

4.4.1 Substitutional diffusion

We first replace a Li and substitute by a T in the layer 1 formed by Li[1], Zr and O. We create also a Li vacancy in the same crystal. The activation energy barrier in this case is calculated to be 0.32 eV. T migrates by forming a bond with O lying close to it as shown in the Figure 18 **a**. We call this as intra-layer diffusion. In similar case but when diffusion of T occurs in the layer 2, activation energy barrier is obtained to be 0.3 eV as shown in the Figure 18 **b**. The experimental result of activation energy barrier for T diffusion in Li_2ZrO_3 is 0.52 eV [15], which is about 0.2 eV off by our calculated minimum energy barrier. When a substituted T from layer 2 diffuses to V_{Li1} (between layer 1 and layer 2) along b direction, we find a resonant transition state exactly in between the V_{Li1} and V_{Li2}. In this case, the barrier is close to zero and T can be stable in between these two vacancies as shown in the Figure 19. But when it diffuses to V_{Li1} along another possible direction as shown in Figure 19 **c**, the barrier is found to be 0.41 eV. The different energy barrier is due to the different O environment that T is subjected to while diffusing.

In case of longer migration path over the distance in which the potential scape changes, energy barriers can also change. We calculate for the case when T diffuses a distance of 4.31 A (layer 1 to layer 2) and 7.16 A (within layer 1) as shown in the Figure 20. In the first case, we obtain energy barrier of 0.45 eV while in the latter case we obtain energy barrier of 1.3 eV. The second migration, particularly, is interesting because it connects two different planes each formed by combining Li[1] and Li[2] layers as shown in the Figure 20.

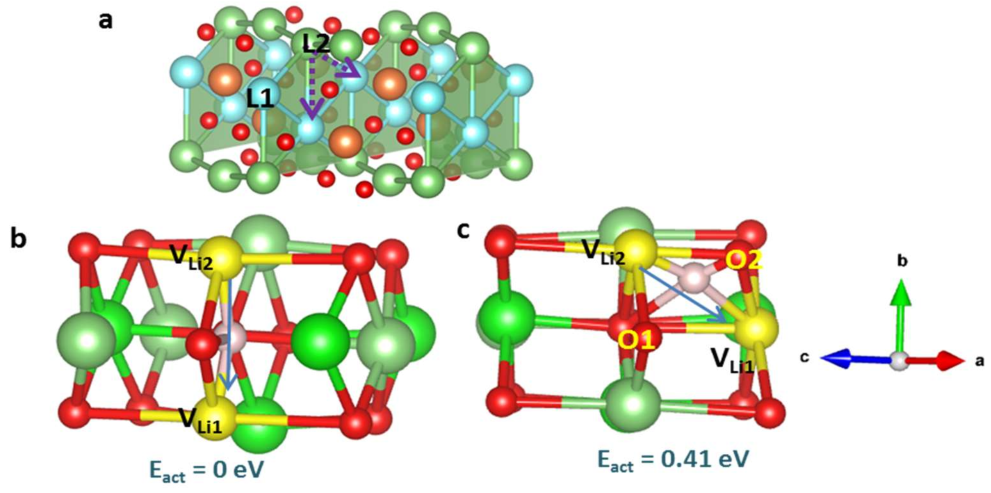

Figure 19 Vacancy assisted migration of T when diffusing from the layer 1 to the Li vacancy located at layer 2. While diffusing along **b** (b) T experiences no barrier but while diffusing to the other direction as shown (**c**), the energy barrier is 0.41 eV.

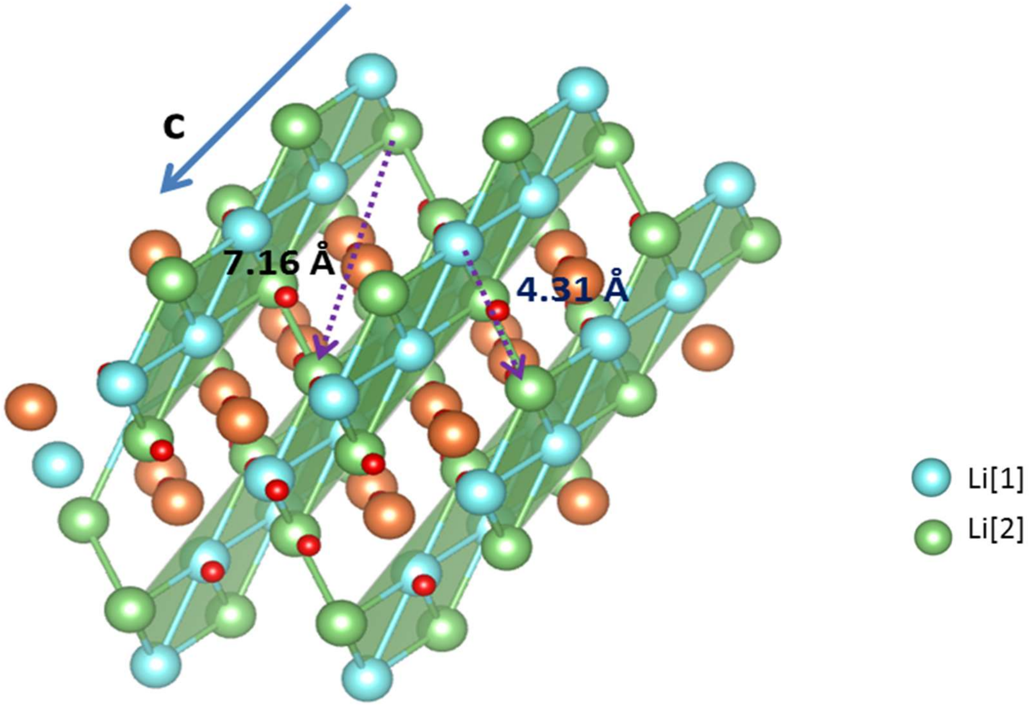

Figure 20 Shaded planes formed by Li[1] and Li[2] layers, oriented along **c**-direction. The long migration of 7.16 Å connects opposite points of two adjacent planes.

4.4.2 Interstitial diffusion

Consider a V_{Li} in the layer 1 and an interstitial T from the layer 2 (a Frenkel defect). The T is diffusing to the V_{Li} (a Frenkel defect) as shown in the Figure 21 **a**. The activation energy barrier is found to be 0.6 eV (Figure 21 **c**) for this case, whereas when T diffuses within the same layer (Figure 21 **b**), it is decreased by almost half (Figure 21 **d**). In previous case, diffusing T atom experiences a repulsive interaction due to change in O environment.

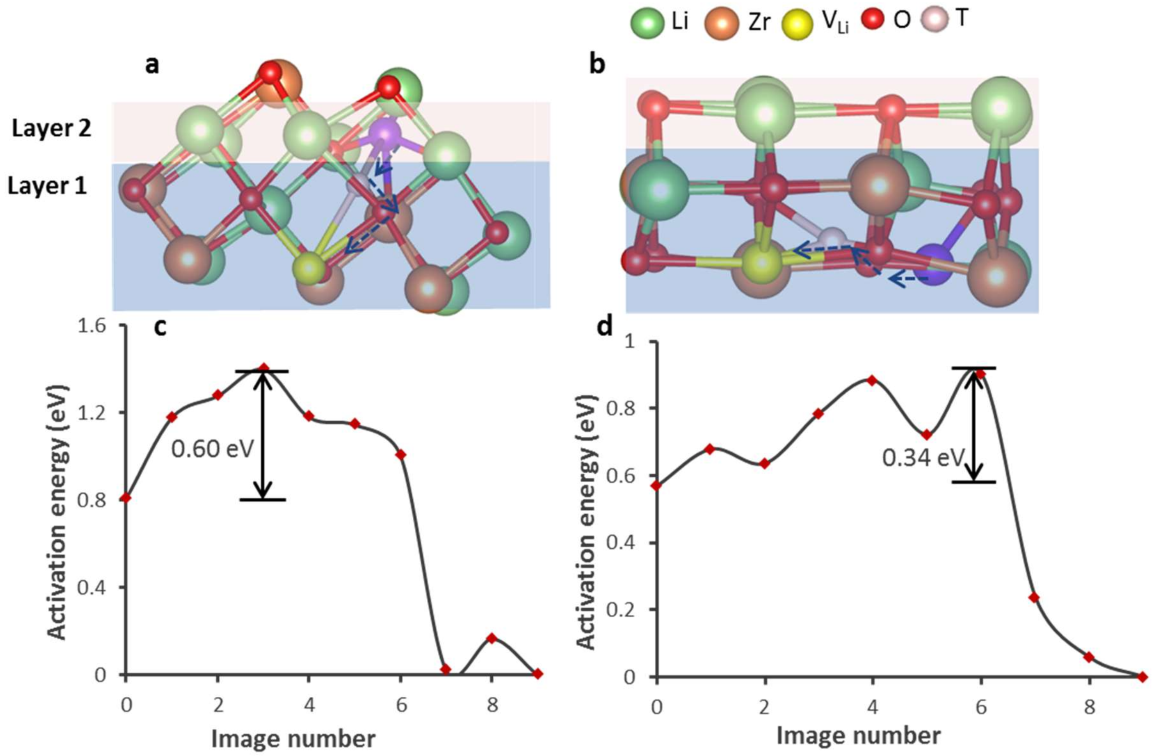

Figure 21 The interstitial migration: T migrates from interstitial position in the layer 2 to V_{Li1} (Frenkel defect recombination) (**a**), and within the same (**b**). The energy barrier in the former case is 0.6 eV, and in the latter case is 0.34 eV.

4.4.3 Bottle neck pathway for T diffusion

A set of parallel strips, with each strip having the Li[1] and Li[2] atoms and extending along c direction and perpendicular to a-c plane, are shown in Figure 22. Two strips are connected by a bottle neck pathway (See Figure 22) between Li[2] atoms in the adjacent strips. The distance between two bridging bottle necks is 5.4 Å. Therefore, mainly the diffusion is dominated by diffusion within a strip. As soon as a Li[2] vacancy is available in the adjacent strip, T makes a jump to recombine with the vacancy as indicated by a narrow cylindrical channel in the Figure 22. The energy barrier for inter-strip migration is found to be 0.3 eV and is a minimum diffusion barrier for Li_2ZrO_3. Our finding is in agreement with the results obtained from the experiment for the Li diffusion in this material as reported in the ref. [16]. The jump between nearest bottle neck pathways is highly unlikely as the energy barrier for that, as discussed in Section 4.4.1, is 1.3 eV which is 1 eV higher than the energy barrier for migration along the bottle neck pathway. As observed in the experiment, at higher temperature jump via the bottle neck pathway can affect significantly to the ionic conductivity. At around 750 K a rise was observed in the ionic conductivity showing that Li atoms are diffusing from one strip to the Li vacancy available in the adjacent strip. Therefore, understanding of diffusion along the bottle neck pathway could be of important for example, in tritium transport experiment where the operating temperature is above 650 K.

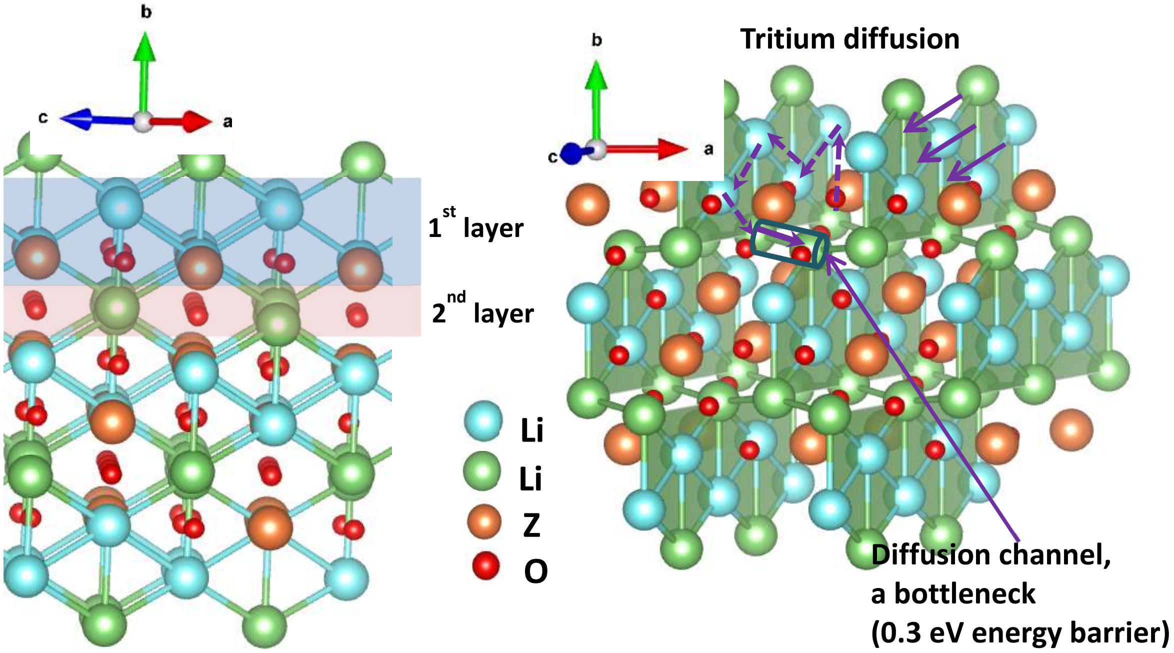

Figure 22 Diffusion of T between two strips happens through a bridge connecting them by two Li[2] atoms. The bridge allows T migration as soon as there is a vacancy available in the adjacent strip. Mainly, diffusion is dominated by a migration within a strip. Unless a Li[2] type vacancy is available in the adjacent strip, it is highly unlikely that inter-strip diffusion is possible.

4.4.4 Diffusion coefficient

In the Figure 23, we present diffusion coefficient calculation using the activation energy of 0.3 eV as a function of temperature. It is to be noted that our calculation gives a qualitative description of the diffusion coefficient. A detail picture of diffusion coefficient requires a calculation of root mean square averaging of atomic position and use Einestien-Smoluchowski equation in molecular dynamics (MD) simulation. The calculated diffusion coefficient at 300 K is 1.2 x 10^{-12} which is 5 orders of magnitude higher than in case of $LiAlO_2$ at the same temperature. At 300 K, there are around 10 million jumps/s whereas at 600 K, it is 4 billion jumps/s.

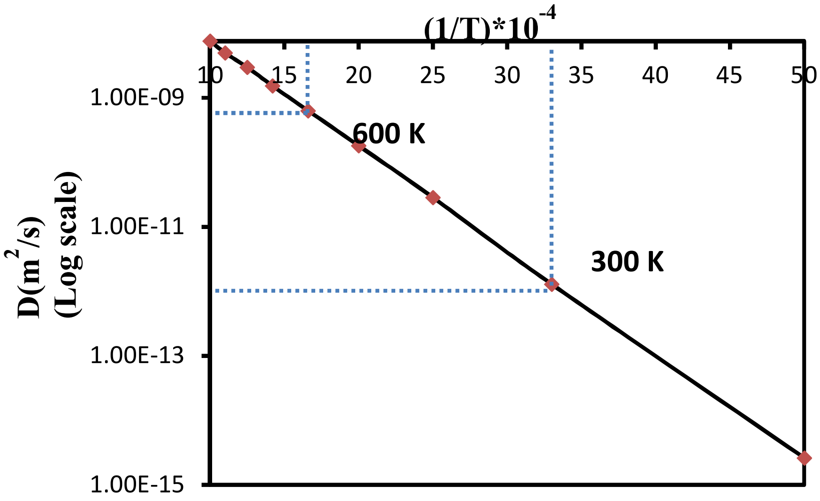

Figure 23 Diffusion coefficient in Log scale for Li_2ZrO_3

4.5 Summary

We studied the diffusion mechanism of ^3T and OT species in order to provide an understanding of the effects on diffusion due to the presence of interstitial and substitutional Li defects, hydroxide (O-T) vacancy defect, and of the interactions of ^3T with O-vacancies in ceramic materials γ- $LiAlO_2$. We considered different diffusion pathways and calculated the activation energy barrier of ^3T and that of O-T as a single bound entity while migrating as interstitial defects or as substitutional defects in a 2x2x2 supercell. Our results showed that the smallest activation energy barrier and the diffusion coefficient are 0.63 eV and 3.25×10^{-12} m^2/s, respectively corresponding to the substitutional ^3T diffusion to the 1st NN Li vacancies in $LiAlO_2$. The smallest energy barrier for OT migration was found to be 2.17 eV corresponding to diffusion to the 1st NN Li vacancies. This diffusion coefficient in this case was calculated to be 3.56×10^{-25} m^2/s. We also studied the correlated motion of T and Li and found that the smallest activation energy barrier is 1.18 eV, and the diffusion coefficient is 3.82×10^{-27} m^2/s, corresponding to Li-T diffusion to the 1st NN position. We also studied the higher order concentration of the defects and ^{3}T in 2x2x2 supercell. But we found that the diffusivities to be several orders of magnitude smaller than single defect in supercell of the same size.

4.6 References

[1] W. Setyawan, D. J. Senor and R. Devanathan, "Atomistic, Insights on Amorphization of Lithium Aluminate from Atomistic Simulation," *J. Phys. Chem. C,* vol. 121, p. 7635, 2017.

[2] M. M. Islam and T. Bredow, "Interstitial Lithium Diffusion Pathways in γ-LiAlO$_2$: A Computational Study," *J. Phys. Chem. Lett.,* vol. 6, p. 4622, 2015.

[3] D. Wiedemann, S. Nakhal, J. J. Rahn, E. Witt, M. M. Islam, S. Zander, P. Heitjans, H. Schmidt, T. Bredow, M. Wilkening and M. Lerch, "Unravelling Ultraslow Lithium-Ion Diffusion in : Experiments with Tracers, Neutron, and Charger Carriers," *Chem. Mater.,* vol. 28, p. 915, 2016.

[4] D. Wohlmuth, V. Epp, P. Bottke, I. Hanzu, B. L.-P. I. Bitschnau, M. Kriechbaum, H. Amenitsch and F. W. M. Hofer, "Order vs. disorder-a huge increase in ionic conductivity of nanocrystalline LiAlO$_2$ embedded in an amorphous-like matrix of lithium aluminate," *J. Mater. Chem. A,* vol. 2, p. 20295, 2014.

[5] S. Indris, P. Heitjans, R. Uecker and B. Roling, "Li Ion Dynamics in a LiAlO2 Single Crystal Studied by 7Li NMR Spectroscopy and Conductivity Measurements," *J. Phys. Chem. C,* vol. 116, p. 14243, 2012.

[6] R. Shah, A. D. Vita, V. Heine and M. C. Payne, "Mechanism of tritium diffusion in lithium oxide," *Phys. Rev. B,* vol. 53, p. 8257, 1996.

[7] R. Shah, A. D. Vita and M. C. Payne, "*Ab initio* study of tritium defects in lithium oxide," *J. Phys. Condens. Matter,* vol. 7, p. 6981, 1995.

[8] J. Perdew, K. Burke and M. Ernzerhof, "Generalized Gradient Approximation Made Simple," *Phys. Rev. Lett.,* vol. 77, p. 3865, 1996.

[9] J. Perdew, K. Burke and M. Ernzerhof, "Generalized Gradient Approximation Made Simple [Erratum Phys. Rev. Lett. 77, 3865 (1996)]," *Phys. Rev. Lett*., vol. 78, p. 1396, 1997.

[10] G. Kresse and J. Hafner, "*Ab initio* molecular dynamics for metals," *Phys. Rev. B*, vol. 47, p. 558, 1993.

[11] G. Kresse and J. Hafner, "*Ab initio* molecular-dynamics simulation of the liquid-metal-amorphous-semiconducotr transiton in germanium," *Phys. Rev. B*, vol. 49, p. 14251, 1994.

[12] P. Shewmon, Diffusion in Solids, Switzerland: Springer International, 2016.

[13] Z. K. Heiba and K. El-Sayed, *J. Appl. Crystallogr.* **35**, 634 (2002).

[14] Y. Duan, “Electronic structural and phonon properties of lithium zirconates and their capabilities of CO$_2$

capture: A first-principle density functional approach", *J. Renew. Sustain. Energy* **3**, 013102 (2011);

[15] Ya.V. Baklanova, I. Yu. Arapova, A. L. Buzlukov, A. P. Gerashenko, S. V. Verkhovskii, K. N. Mikhalev, T. A. Denisova, I. R. Shein, L. G. Maksimova, "Localization of vacancies and mobility of Lithium ions in Li_2ZrO_3 as obtained by ^{6,7}Li NMR", *J. Solid State Chem*. **208** (2013) 43–49

[16] E. A. Sherstobitova, A. F. Gubkin, I. A. Bobrikov, A. V. Kalashnov, M. I. Pantyukhina, "Bottle-necked ionic transport in Li_2ZrO_3: high temperature neutron diffraction and impedance spectroscopy", *Electrochimica Acta* **209** (2016) 574–581

5. Summary and further work

By using density functional theory (DFT), in this study, we investigated the solubility and diffusivity properties of tritium ($^{3}_{1}T$) in the blanket candidate materials $LiAlO_2$ and Li_2ZrO_3 for TPBARs to enable $^{3}_{1}T$ production in PWRs and to enhance the performances of these components.

The blanket material $LiAlO_2$ is stable at high temperatures, characteristic that enables an efficient production of $^{3}_{1}T$. In this porject we focused to identify the mechanisms associated with atomic $^{3}_{1}T$ formation, diffusion, transport, deposition, and the kinetics at high temperature.

Using a combined DFT and lattice phonon dynamics approach, we calculated the electronic, optical, thermal conductivity, and thermodynamic properties of γ-$LiAlO_2$ and ^{6}Li isotope substituted γ-$^{6}LiAlO_2$. After substituting ^{7}Li with ^{6}Li isotope in γ-$LiAlO_2$, the lattice phonon frequencies have changed, and modifications in the range 5-15 THz out of entire frequency spectra (0-26 THz) have been evidenced. We have also calculated the lattice thermal conductivity by taking anharmonic effects into account in the calculations. Our results were found to be in good agreement over a wide range of temperature with the available experimental data. As the temperature increases, it was found that the phonon free energies for both γ-$LiAlO_2$ and ^{6}Li isotope substituted γ-$^{6}LiAlO_2$ were decreased while their entropies were increased.

We systematically studied the defect stability as a function of electron chemical potential under two selected chemical potential conditions (oxygen-rich and metal hydride rich conditions) for the materials the γ-$LiAlO_2$, Li_2ZrO_3, and Li_2TiO_3. The calculated defect stability results were in good agreement with the previous works. The consistent thermodynamic analysis using the PyCDT module of pymatgen allowed to extract defect stability information for comparison among the selected materials systems. Overall H_O formation energy trend under the metal hydride rich condition (also the oxygen rich condition) is as follows: γ-$LiAlO_2 > Li_2ZrO_3 > Li_2TiO_3$.

In this work, we have also studied the diffusion mechanism of T and OT species in order to provide an understanding of the effects on diffusion due to the presence of interstitial and substitutional Li defects, hydroxide (O-T) vacancy defect, and of the interactions of T with O-vacancies in ceramic materials γ-$LiAlO_2$ and Li_2ZrO_3. By considering several different diffusion pathways, we calculated the activation energy barrier of T as well as of O-T as a single entity while migrating as interstitial defects or as substitutional defects. Our results show that the smallest activation energy barrier is 0.63 eV corresponding to the substitutional T diffusion in $LiAlO_2$ while it is 0.3 eV in Li_2ZrO_3.

In future, two major avenues can be chosen to explore further the diffusion mechanisms in blanket materials. First, it still need to explore the effects of O, Al, Zr defects on the ^3_1T diffusivity and solubility in γ-$LiAlO_2$ and Li_2ZrO_3. After irradiation, due to an enormous amount of kinetic energy of neutron beams, the recoiled helium nuclei can create defect rich regions within surface grain boundaries. These defects can trap or slow down the released molecular ^3_1T which may have different diffusion mechanism. Second, it is essential to understand the surface and interface diffusion mechanisms of various chemical species such as T, OT^-, and H2O. Once the ^3_1T diffuses from the bulk to the surface/interface, surface chemistry plays an important role. The mechanisms such as adsorption/desorption and recombination/dissociation at given temperatures are key factors controlling formation of ^3_1T. In addition to these, the lattice oxygen could become bonded to ^3_1T, leading to formation of T_2O or OT^- species on γ-$LiAlO_2$ surface, from where desorption can take place. These studies could provide a further understanding of the various physical and chemical processes occurring in the blanket materials, and hence assist in modelling and to improve the performance of TPBAR systems.

6. Acknowledgements

This research is supported by the Tritium Science Program under National Nuclear Security Administration (NNSA). H. P. & Y.-L. L. thanks the National Energy Technology Laboratory Research and Innovation Center providing Computational resources administered by the Oak Ridge Institute for Science and Education (ORISE). J. H. Y.-L.L. thanks the DOE MELF Summer Internship. We thank the Tritium Science Program Manager, Dr. David Senor (PNNL), for his excellent managemental skills and helpful comments on this work. We also thank Drs. Weilin Jiang and Ram Devanathan (PNNL) for fruitful discussions and suggestions. We thank NETL management officers (Dr. Michael Nowak, Christy L. Pecyna, Steven Richardson) for their excellent guidelines and help. The views and opinions of authors expressed herein do not necessarily state or reflect those of the United States Government or any agency hereof.